



Uppermost mantle velocity beneath the Mid-Atlantic Ridge and transform faults in the equatorial Atlantic Ocean

Guilherme Weber Sampaio de Melo, Ross Parnell-Turner, Robert Dziak, Deborah Smith, Marcia Maia, Jean-Yves Royer

► To cite this version:

Guilherme Weber Sampaio de Melo, Ross Parnell-Turner, Robert Dziak, Deborah Smith, Marcia Maia, et al.. Uppermost mantle velocity beneath the Mid-Atlantic Ridge and transform faults in the equatorial Atlantic Ocean. Bulletin of the Seismological Society of America, 2020, 111 (2), pp.1067-1079. hal-03062624

HAL Id: hal-03062624

<https://hal.science/hal-03062624>

Submitted on 14 Dec 2020

HAL is a multi-disciplinary open access archive for the deposit and dissemination of scientific research documents, whether they are published or not. The documents may come from teaching and research institutions in France or abroad, or from public or private research centers.

L'archive ouverte pluridisciplinaire **HAL**, est destinée au dépôt et à la diffusion de documents scientifiques de niveau recherche, publiés ou non, émanant des établissements d'enseignement et de recherche français ou étrangers, des laboratoires publics ou privés.

Bulletin of the Seismological Society of America

Uppermost mantle velocity beneath the Mid-Atlantic Ridge and transform faults in the equatorial Atlantic Ocean --Manuscript Draft--

Manuscript Number:	BSSA-D-20-00248R5
Article Type:	Article
Section/Category:	Regular Issue
Full Title:	Uppermost mantle velocity beneath the Mid-Atlantic Ridge and transform faults in the equatorial Atlantic Ocean
Corresponding Author:	Guilherme Weber Sampaio de Melo, M.D. Federal University of Rio Grande do Norte Natal, Rio grande do norte BRAZIL
Corresponding Author's Institution:	Federal University of Rio Grande do Norte
Corresponding Author E-Mail:	gwsmelo@ufrn.edu.br
Order of Authors:	Guilherme Weber Sampaio de Melo, M.D. Ross Parnell-Turner Robert P. Dziak Deborah K. Smith Marcia Maia Aderson F. do Nascimento Jean-Yves Royer
Abstract:	<p>Seismic rays travelling just below the Moho provide insights into the thermal and compositional properties of the upper-mantle, and can be detected as Pn phases from regional earthquakes. Such phases are routinely identified in the continents, but in the oceans, detection of Pn phases is limited by a lack of long-term instrument deployments. We present estimates of upper-mantle velocity in the equatorial Atlantic Ocean from Pn arrivals beneath, and flanking, the Mid-Atlantic Ridge, and across several transform faults. We analyzed waveforms from 50 earthquakes with magnitude $MW > 3.5$, recorded over 12 months in 2012–2013 by five autonomous hydrophones and a broadband seismograph located on the St. Peter and St. Paul archipelago. The resulting catalog of 152 ray paths allows us to resolve spatial variations in upper-mantle velocities, which are consistent with estimates from nearby wide-angle seismic experiments. We find relatively high velocities near to the St. Paul transform system (~ 8.4 km s⁻¹), compared to lower ridge-parallel velocities (~ 7.7 km s⁻¹). Hence, this method is able to resolve ridge-transform scale velocity variations. Ray paths in lithosphere younger than 10 Myr have mean velocities of 7.9 ± 0.5 km s⁻¹, which is slightly lower than those sampling lithosphere older than 20 Myr (8.1 ± 0.3 s⁻¹). There is no apparent systematic relationship between velocity and ray azimuth, which could be due to thickened lithosphere or complex mantle upwelling, although uncertainties in our velocity estimates may obscure such patterns. We also do not find any correlation between Pn velocity and shear wave speeds from the global SL2013sv model at depths < 150 km. Our results demonstrate that data from long-term deployments of autonomous hydrophones can be used to obtain rare and insightful estimates of uppermost mantle velocities over hundreds of kilometers, in otherwise inaccessible parts of the deep oceans.</p>
Author Comments:	
Suggested Reviewers:	Rachel Abercrombie Boston University rea@bu.edu Seismology expert with interests in equatorial Atlantic Emilie Hooft

	University of Oregon emilie@uoregon.edu Seismology expert with interests in upper mantle structure
	John Collins Woods Hole Oceanographic Institution jcollins@whoi.edu Seismology expert with interest in passive methods
Opposed Reviewers:	
Response to Reviewers:	
Additional Information:	
Question	Response
Key Point #1: Three key points will be printed at the front of your manuscript so readers can get a quick overview. Please provide three COMPLETE sentences addressing the following: 1) state the problem you are addressing in a FULL sentence; 2) state your main conclusion(s) in a FULL sentence; and 3) state the broader implications of your findings in a FULL sentence. Each point must be 110 characters or less (including spaces).	Upper mantle velocity structure is important, but difficult and expensive to measure in remote ocean basins
Key Point #2:	Pn arrivals detected by autonomous hydrophones constrain upper mantle velocity in equatorial Atlantic Ocean
Key Point #3:	No azimuthal dependence of VPn, could be due to thickened lithosphere, or complex mantle upwelling



Uppermost mantle velocity beneath the Mid-Atlantic Ridge and transform faults in the equatorial Atlantic Ocean

Guilherme W. S. de Melo, Ross Parnell-Turner, Robert P. Dziak, Deborah K. Smith,
Marcia Maia, Aderson F. do Nascimento, and Jean-Yves Royer

Abstract

Seismic rays travelling just below the Moho provide insights into the thermal and compositional properties of the upper-mantle, and can be detected as Pn phases from regional earthquakes. Such phases are routinely identified in the continents, but in the oceans, detection of Pn phases is limited by a lack of long-term instrument deployments. We present estimates of upper-mantle velocity in the equatorial Atlantic Ocean from Pn arrivals beneath, and flanking, the Mid-Atlantic Ridge, and across several transform faults. We analyzed waveforms from 50 earthquakes with magnitude $M_w > 3.5$, recorded over 12 months in 2012–2013 by five autonomous hydrophones and a broadband seismograph located on the St. Peter and St. Paul archipelago. The resulting catalog of 152 ray paths allows us to resolve spatial variations in upper-mantle velocities, which are consistent with estimates from nearby wide-angle seismic experiments. We find relatively high velocities near to the St. Paul transform system ($\sim 8.4 \text{ km s}^{-1}$), compared to lower ridge-parallel velocities ($\sim 7.7 \text{ km s}^{-1}$). Hence, this method is able to resolve ridge-transform scale velocity variations. Ray paths in lithosphere younger than 10 Myr have mean velocities of $7.9 \pm 0.5 \text{ km s}^{-1}$, which is slightly lower than those sampling lithosphere older than 20 Myr ($8.1 \text{ km} \pm 0.3 \text{ s}^{-1}$). There is no apparent systematic relationship between velocity and ray azimuth, which could be due to thickened lithosphere or complex mantle upwelling, although uncertainties in our velocity estimates may obscure such patterns. We also

do not find any correlation between P_n velocity and shear wave speeds from the global SL2013sv model at depths < 150 km. Our results demonstrate that data from long-term deployments of autonomous hydrophones can be used to obtain rare and insightful estimates of uppermost mantle velocities over hundreds of kilometers, in otherwise inaccessible parts of the deep oceans.

Introduction

Seismic velocity measurements provide a useful tool for investigating spatial variations in upper-mantle properties, such as temperature and anisotropy, with implications for melt supply and mantle heterogeneity (e.g. Lin and Phipps Morgan, 1992; Dunn *et al.*, 2005). These measurements are relatively straightforward to obtain on the continents (e.g. Chulick and Mooney, 2002; Chulick *et al.*, 2013). However, it remains challenging and expensive to measure upper-mantle seismic velocity in the deep ocean, due to its remote location and difficulties in deploying long-term instruments on the seafloor. P_n phases are rays that are critically refracted at the Moho and propagate along the top of the uppermost mantle (e.g. Linehan, 1940; Brandsdottir and Menke, 1997). At the Mid-Atlantic Ridge (MAR) from 10°N to 35°N , P_n arrivals from 48 individual ray paths were recorded with hydrophones, and used to investigate upper-mantle velocities, giving a mean velocity of 8.0 ± 0.1 km s $^{-1}$ (Dziak *et al.*, 2004). This velocity estimate was higher than that from nearby active source seismic experiments along the ridge axis ($7.5\text{--}7.9$ km s $^{-1}$; Canales *et al.*, 2000), probably due to the effects of younger and thinner oceanic lithosphere being sampled by the refraction profiles, and the effects of averaging velocities across all rays. Despite such advances, upper-mantle velocities in the deep oceans remain poorly constrained, and the potential for hydrophone-recorded P_n phases to resolve

spatial variations in upper-mantle velocity has not yet been sufficiently tested.

Here, we use *Pn* arrivals from regional earthquakes to constrain upper-mantle velocity in the equatorial Atlantic Ocean. Arrivals were recorded by a combination of five moored hydrophones and a single seismograph station installed on the St. Peter and St. Paul islets, giving 152 ray paths that sample mantle conditions both on- and off-axis, and across the St. Paul transform system. Our study is coincident with several mantle velocity estimates from a wide-angle seismic experiment (Le Pichon *et al.*, 1965), and hence has the opportunity to validate spatial variations in velocity revealed by groups of similar ray paths.

Equatorial Atlantic Ocean

In the equatorial Atlantic Ocean (10°N–5°S and 34°W–21°W), the MAR is offset by some of the longest transform faults on Earth, including the Strakhov, St. Paul, and Romanche transforms (Figure 1). The St. Paul transform system consists of four transform faults and three intra-transform ridge segments that accommodate an offset of 630 km. The northwest transform fault is currently undergoing transpression, giving rise to the ~200 km-long and ~30 km-wide Atobá ridge (Maia *et al.*, 2016), and also uplift of 1.5mm yr⁻¹ at the St. Peter and St. Paul islets (Campos *et al.*, 2010; Maia *et al.*, 2016). Other transforms in the system do not host topographic highs or an island related to transpression, and hence presumably are not experiencing uplift. In the three intervening spreading segments, seafloor spreading is slow, at ~16 mm yr⁻¹ average half rate (DeMets *et al.*, 2010). Faulting plays an important role in crustal accretion, and seismicity rates are relatively high, providing a useful tool to investigate the properties of the crust and upper mantle, as well as deformation at long-offset strike-slip systems (e.g. Francis *et al.*, 1978; Abercrombie and Ekstrom, 2001; de Melo and do Nascimento, 2018).

Methods

Waveform Data

We analyzed *Pn* arrivals in waveform data recorded by a combination of five moored autonomous hydrophones and one land-based seismograph (Figure 2). The five autonomous hydrophone instruments were deployed during two separate experiments: stations EA2 and EA8 were part of the Equatorial Atlantic (EA) array (Smith et al., 2012). Data were recorded at 16-bit resolution and a sampling rate of 250 Hz; for further details on these hydrophone instruments see Fox *et al.* (2001). Hydrophones H2, H4, H5 were deployed during the COLd Mantle Exhumation and Intra-transform Accretion experiment (COLMEIA; Maia *et al.*, 2014, 2016), and recorded data at 24 bit-resolution with a sampling rate of 240 Hz; for further instrument details see D’Eu *et al.* (2012). We also used waveform data recorded by a three-component broadband seismograph installed at the St. Peter and St. Paul Archipelago Scientific Station on the Belmonte islet (ASPSP; de Melo and do Nascimento, 2018). This station is operated by the Seismological Laboratory of Federal University of Rio Grande do Norte in cooperation with the Brazilian Navy. The sparse distribution and mixed instrument types we used means that data coverage is uneven, as shown in Figure 1b. Waveform data were examined for the time period from July 2012 to July 2013, with recording intervals dictated by technical challenges and vessel schedules (Figure 1b).

Pn analysis

Prior to manually picking *Pn* arrivals, we applied a 6–20 Hz Butterworth bandpass filter to the hydrophone data in order to suppress unwanted noise. A bandpass filter with range 4–12 Hz was applied prior to picking arrivals from the ASPSP seismograph, to suppress additional

microseism noise due to its island location. Based upon origin time, events were manually associated with earthquakes in the International Seismological Center Bulletin (ISC), yielding hypocenter locations, origin times, and magnitudes ranging from 3.5 to 5.4 M_w . Earthquakes mostly occur due to strike-slip faulting along the Strakhov, St. Paul, and Romanche transform faults, with additional events due to extension along the intervening spreading ridge segments (Figure 2a). Example arrivals from three events are shown in Figures 3 and 4, highlighting the typical response to strike-slip and normal faulting earthquakes ranging in magnitude from 4.6 to 5.3 M_w .

Typical Pn -arrivals are emergent, and have low signal-to-noise ratio (SNR; noted in Figures 3 and 4), making pick identification challenging. Given the mixed nature of our network and often noisy arrivals, picks were made based on the onset of emergent energy combined with changes in SNR, waveform character and amplitude. The observation of linear move-out, consistent with upper mantle velocity, added confidence to our picks, since this moveout is evident across the hydrophone array stations due to wave propagation along the crust-mantle interface (see common-receiver plots in Supplementary Figures S1–S6). P -arrivals are easily distinguished from T -phase arrivals, which arrive much later than P -arrivals, are emergent in character, and are higher in amplitude than P -arrivals (see hydrophone H5 in Figure 4). The catalog of detected events is given in Table S1.

In order to further test whether the detected arrivals were Pn phases, we compared the observed travel times to those predicted by the global iasp91 velocity model (Kennett and Engdahl, 1991). For each source-receiver ray path, we calculated the predicted Pn arrival time using iasp91, with the addition of a station-dependent delay to account for the propagation time from seafloor to hydrophone. This delay (1.2–2.5 s, see Table 1) was estimated using the

hydrophone mooring cable length at each station, and the local water sound velocity estimated from the Global Ocean Sound Speed Profile Library (Barlow, 2019). The predicted Pn arrival times differ from the observed Pn arrivals by 5–10 s (Figures 3 and 4), a difference which arises since the iasp91 model contains a crustal layer that is much thicker (30 km) than that expected in the oceans (~6 km). Hence, the differences in observed and predicted Pn arrival time are probably dominated by this additional crustal layer thickness in the velocity model, plus earthquake location and origin time uncertainties. Although these differences are evident, the waveform character and linear move-out velocity give us confidence in our identification of these emergent phases as Pn arrivals.

ISC origin times were subtracted from the Pn arrival times to obtain travel times for each ray path (i.e. each event-station pair). We account for travel time in the oceanic crust by subtracting ray path distances and travel times for the portion of the path that travels through the crust, assuming that all events occurred at 10 km depth (ISC catalog), and that crustal thickness is uniformly 6.0 km with a crustal velocity of 6.5 km s⁻¹ (Christeson *et al.*, 2019). For each station, we then calculate the distance and travel time for the portion of the ray path that extends from an earthquake in the crust to the Moho, and back from the Moho to the receiver. Pn velocity is obtained by dividing the distance travelled in the mantle by the travel time in the mantle. Details of these corrections for each station are given in Table 1.

Our approach yielded 152 Pn velocity estimates from the catalog of 50 regional earthquakes (Figure 5). Although epicentral distances range from 32 km to ~1095 km, all 50 events were detected at nearly all available stations, implying that the detection threshold of the combined hydrophones and ASPSP station is at least M_w 3.5. Since most stations were located either near to, or to the north of, the St. Paul fracture zone, our ray path coverage is more

comprehensive in the northern part of the study area. Ray paths sampling upper-mantle velocities to the south of the St. Paul fracture zone are restricted to events detected by hydrophone EA8, and those originating from four earthquakes located at the eastern end of the Romanche transform fault (Figure 5).

Pn velocity uncertainty

The two most significant potential sources of error in our analysis are hypocenter locations of events in the ISC Catalog, and *Pn* arrival time picks. We estimated hypocenter location (and hence epicentral distance) error to be ± 10 km, based upon ISC catalog location and typical error in global earthquake location (Lohman and Simons, 2005; Weston *et al.*, 2012). This hypocenter location error implicitly includes other uncertainties associated with ISC catalog locations, such as those caused by un-modeled three-dimensional velocity structure and picking errors, which result in trade-offs between origin time and location (Bondár and Storchak, 2011). Arrival time pick (and hence also travel time) errors were investigated by estimating SNR for each arrival via two methods, one using the amplitude ratio between peak signal and root mean square noise, and another via the ratio between the short time average amplitude and long time average amplitude (STA/LTA; Figure S7). We find that both SNR estimates are only weakly dependent on epicentral distance and magnitude, however we do observe station-dependent variations in the scatter in SNR. We quantify this scatter in terms of the standard deviation of SNR of arrivals for a particular station (Figure S7e), which likely is due to persistent local noise sources. Hence we estimated arrival time pick error based on the emergent character of arrivals and the standard deviation of SNR, with station-dependent errors defined as ± 0.5 s for EA2 and EA8; ± 1.0 s for H2, H4 and H5; and ± 0.3 s for ASPSP.

The total uncertainty in our velocity estimate, δv , was estimated by assuming that epicentral distance, d , and travel time, t , have errors that are uncorrelated and random. This assumption is valid since we attribute the main source of travel time error to uncertainty in picking of Pn arrivals (which in turn depends on waveform character and noise level), and the distance error is most significantly affected by error in earthquake location from the ISC catalog, which is assumed to be constant and hence is independent from hydrophone Pn pick error. We formally propagate the errors in d and t , as follows

$$\delta v = v \sqrt{\left(\frac{\delta d}{d}\right)^2 + \left(\frac{\delta t}{t}\right)^2},$$

where δd is epicentral distance error, and δt is travel time error (e.g. Taylor, 1997).

Although receiver location uncertainty is negligible for the land station ASPSP (located with meter-scale accuracy via the Global Positioning System), there is potential location uncertainty for the moored hydrophones in our network. Moored hydrophone locations were obtained by acoustic triangulation between the mooring acoustic release and the deployment vessel soon after the moorings settled on the seafloor, within error of several meters. In order to account for the possibility of abnormally strong current motion, each instrument was fitted with a pressure and temperature logger below the floatation package, so that any significant hydrophone depth changes would be recorded (e.g. Fox *et al.*, 2001). Significant depth changes were not detected during depolyments, and thus we assume that the hydrophone location was constant during data collection, and hence hydrophone location uncertainty is less than 10 m.

184

185 **Results**186 ***Pn* velocities**

187 The resulting 152 *Pn* ray paths (Figure 5b) and travel times (Figure 6) indicates upper-
188 mantle velocities that vary considerably across the study area, with estimates ranging between
189 7.2 and 11.1 km s⁻¹, and uncertainties ranging from 0.1 to 1.9 km s⁻¹ (Table S2). Variability in
190 reduced travel time increases with epicentral distance (Figure 6), although SNR does not show a
191 similar trend (Figure S7). Hence the epicentral distance-dependent scatter in reduced travel time
192 is likely due to variations in the depth of ray penetration (which increases with epicentral
193 distance), and not due to increasing pick uncertainty. At the center of the study area there
194 appears to be a longitudinal variation in *Pn* velocity, with events originating near the St. Paul
195 transform system, and sampling adjacent lithosphere, having higher velocities than those from
196 the adjacent spreading centers (Figure 5a). The best constrained estimate for sub-axis, ridge-
197 parallel mantle velocity comes from ray paths that sample the portion of the spreading axis
198 between the Strakhov fracture zone and stations near the St. Paul fracture zone (H2, H5 and
199 ASPSP). Here, *Pn* travel times consistently imply relatively low velocities, with a mean of 7.7
200 km s⁻¹. Slightly higher velocities ranging between 7.8 and 8.2 km s⁻¹ are indicated by ray paths
201 between hydrophone EA2 and the Strakhov fracture zone, oriented roughly parallel to a plate
202 spreading flowline. Ray paths oriented southwest-northeast (azimuth ~060°), i.e. oblique to the
203 spreading direction, between events on the St. Paul fracture zone and detected at hydrophone
204 EA2, have some of the highest mantle velocities (between 7.6 and 8.5 km s⁻¹) compared to other
205 rays sampling areas unaffected by fracture zones. Velocity estimates in the vicinity of the St.
206 Paul fracture zone itself (from transform faulting events detected by hydrophones H2, H4 and

H5, and ASPSP) show considerable variation, ranging from 8.0 to 9.1 km s⁻¹ and a mean of 8.4 km s⁻¹, and little apparent spatial consistency. Among these events, we encountered one of the highest *Pn* velocities (9.0 km ± 0.2 s⁻¹) in this study, for a ray path oriented roughly parallel to the St. Paul transform fault (ray azimuth ~105°) between an event near the St. Paul islets and detected by hydrophone H4.

South of the St. Paul fracture zone, ray paths from events detected by hydrophone EA8 showed considerable variation in upper-mantle velocity, which range from 7.2 to 9.0 km s⁻¹. Ray paths originating from the spreading axis north of the St. Paul transform fault and trending ~170° towards EA8, have velocities of 7.3–8.1 km s⁻¹, while ray paths from the St. Paul transform fault trending ~185° towards EA8 have consistently higher velocities of 7.6–9.1 km s⁻¹.

Only 12 ray paths sampling the upper-mantle parallel and adjacent to the spreading axis between the southern extent of the St. Paul transform fault and the Romanche transform fault are available. This relatively poor coverage in ray paths in this area hinders our interpretation, where velocities range from 7.2 to 8.3 km s⁻¹.

Discussion

Upper-mantle velocity structure

In general, rays originating from the St. Paul transform system have higher velocities than those originating from active spreading centers to the east and west (Figure 5a), probably due to cooler conditions at the Moho along the transform. Our estimates of upper-mantle *Pn* velocities broadly agree (within error) with *Pn* velocities from radially stratified velocity models such as PREM (Dziewonski and Anderson, 1981) and iasp91 (Figure 6; Kennett and Engdahl, 1991). Our *Pn* velocity estimates are also consistent with mantle velocity estimates from a series of

reversed wide-angle refraction seismic profiles (i.e. with multiple shot points giving overlapping coverage) collected in the equatorial Atlantic during R/V *Atlantis* cruise A180 (Figure 5b; Le Pichon *et al.*, 1965). The modal difference in velocity between refraction profiles from Le Pichon *et al.* (1965) and all intersecting ray paths is 0.2 km s^{-1} (see histogram in Figure 5c), although our *Pn* velocity estimates are consistently lower than those reported by Le Pichon *et al.* (1965), with a maximum disagreement of 1.2 km s^{-1} . A mantle velocity of 8.30 km s^{-1} was reported along profile A180-48, which is 283 km-long, and crosses the eastern side of the St. Paul transform fault (near $\sim 26.3^\circ\text{W}$), trending northeast-southwest (Figure 5b). This velocity is consistent with that inferred from *Pn* ray paths with a similar orientation, originating from earthquakes on the St. Paul transform fault that were detected by hydrophone EA8. Ray paths that intersect profile A180-48 (at angles either perpendicular or oblique to the trend of the refraction profile) typically indicate lower upper-mantle velocities, ranging from 7.3 to 8.1 km s^{-1} , with the exception of one anomalous ray path oriented parallel with the St. Paul transform fault with a velocity of 9.0 km s^{-1} . Refraction profiles A180-40 and -42 are oriented roughly east-west, are located ~ 100 km north of the Romanche transform fault, and have velocities of 8.03 and 8.49 km s^{-1} , respectively. Although there are only four *Pn* ray paths near to these profiles, with near-perpendicular orientation, they indicate velocities ranging from 7.6 to 8.2 km s^{-1} , and hence are in broad agreement with the refraction estimates. Our velocity estimates of 7.6 to 8.2 km s^{-1} are also in agreement with a velocity estimate of 8.0 km s^{-1} from an active source experiment near 18°W roughly perpendicular to the St. Paul fracture zone, which at this longitude separates 40 Myr old crust in the south from 70 Myr old crust in the north (Grove *et al.*, 2019). The general agreement between upper-mantle velocities from the refraction profiles

and our *Pn* arrivals validates our results, and implies that spatial trends observed in the study area are likely to be real.

Elsewhere along the MAR, between 10° to 40°N, a mean upper-mantle velocity of $8.0 \text{ km} \pm 0.1 \text{ km s}^{-1}$ was estimated using a similar method to this study with *Pn* arrivals detected by an array of autonomous hydrophones (Dziak *et al.*, 2004). Ray paths used by Dziak *et al.*, (2004) often crossed the ridge axis, spanned a series of fracture zones, and extended onto older crust, which may explain the close agreement in results. This result suggests that off-axis and on-axis upper mantle characteristics are similar in the northern and equatorial Atlantic Ocean.

Near the Oceanographer transform fault on the MAR (~35°N), a two-dimensional tomographic inversion of wide-angle seismic refraction data suggests velocities of $7.4\text{--}7.8 \text{ km s}^{-1}$ (Canales *et al.*, 2000; Hooft *et al.*, 2000). These results agree within error with our estimates of *Pn* velocity from rays sampling on-axis upper-mantle to the north of the St. Paul transform fault (Figure 5b), which are typically $7.2\text{--}8.0 \text{ km s}^{-1}$.

Upper-mantle velocity and plate age

Seismic velocities in the upper-mantle near to the ridge axis, i.e. in young lithosphere, are expected to be lower than in off-axis areas, due to upwelling of hot material (e.g. Turcotte and Schubert, 2002). Following the removal of minor gridding artifacts associated with fracture zone traces, we used a global crustal age model (Müller *et al.*, 2008) to assign a mean crustal age along each ray path, for comparison with *Pn* velocity (Figure 7a).

Ray paths sampling lithosphere younger than 10 Myr show a wide range of velocities, with a mean of 7.9 km s^{-1} and standard deviation of 0.5 km s^{-1} . Twenty ray paths yield velocities less than 7.5 km s^{-1} . *Pn* velocities for ray paths sampling lithosphere older than 20 Myr are

slightly higher, with a mean of 8.1 km s^{-1} and standard deviation of 0.3 km s^{-1} , while only two ray paths give velocities lower than 7.5 km s^{-1} (Figure 7a). Most rays cover a wide range of crustal ages, so this geometry, and our averaging approach, may smear the possible effects of lithospheric aging. The lack of rays travelling exclusively via older lithosphere may also obscure any progressive trend between upper-mantle velocity and crustal age. However, the tendency toward the inclusion of lower velocities in younger crust (Figure 7a) reflects the expected variation with respect to the zone of axial upwelling.

Azimuthal Seismic Anisotropy

Laboratory experiments have shown that the mantle can experience significant shear strain during corner flow at the ridge axis, leaving an anisotropic fabric in the lithospheric mantle as minerals (e.g. olivine) are aligned into a lattice preferred orientation (LPO; e.g. Zhang and Karato, 1995; Nicolas and Christensen, 2011). Anisotropy consistent with a LPO formed by two-dimensional mantle flow has been measured at some locations in the oceanic upper mantle, in particular at the fast-spreading East Pacific Rise (e.g. Raitt *et al.*, 1969; Lin *et al.*, 2016), however the strength of anisotropy varies widely, and debate remains about its origins (e.g. Mark *et al.*, 2019). Since isochrons in this region are fairly uniform (Figure 5), V_{Pn} anisotropy could be expected parallel to paleo-relative plate motion, although this assumption has been shown to not apply everywhere (VanderBeek and Toomey, 2017).

We investigated the dependence of mantle velocity with azimuth, and use epicentral distance as a proxy for depth of mantle penetration to group rays (Figure 7b). No discernable pattern is evident in rays grouped by epicentral distance, including those expected to sample deepest in the mantle with epicentral distances $> 700 \text{ km}$ (blue lines in Figure 7c). Removing

rays with V_{Pn} error $> 0.4 \text{ km s}^{-1}$ also does not resolve any azimuthal dependence (Figure 7d), nor does separating rays by mean crustal age (Figures 7e and 7f).

The apparent lack of such azimuthal dependence could be due to several reasons. First, azimuthal dependence may be too subtle to be resolved by our V_{Pn} estimates, given the uncertainties in hypocenter location and crustal thickness discussed above. Second, the slow spreading rate of the MAR ($\sim 32 \text{ mm yr}^{-1}$ total rate; (DeMets *et al.*, 2010)) may result in a thickened lithosphere that is dominantly cooled by conduction, thus inhibiting corner flow (e.g. Sleep, 1975). As a result, deformation could be accommodated by faulting at depths of 5–10 km beneath the Moho, reducing the viscous strain in the mantle at these depths, and suppressing the anisotropy recorded in the mantle (e.g. Ribe, 1989). Observations of weaker or anomalous anisotropy elsewhere in the Atlantic Ocean are consistent with our findings (e.g. Gaherty *et al.*, 2004; Dunn *et al.*, 2005). Third, complex, three-dimensional upwelling patterns near the ridge axis could result in anisotropy on relatively short wavelengths (Lin and Phipps Morgan, 1992), which would be smeared along our relatively long ray paths, and hence not be resolved.

Pn and surface wave velocity

To explore the relationship between V_{Pn} and the thermal structure of the asthenospheric upper-mantle, we compared our velocity estimates with a global, vertically polarized shear speed model SL2013sv (Schaeffer and Lebedev, 2013). Our objective is to evaluate our observations of uppermost mantle properties in the context of deeper mantle properties. We do not aim to directly validate our V_{Pn} estimates via this comparison. This model was chosen because it is particularly sensitive to anomalies within the upper-mantle, and hence provides a window into the upper mantle structure directly beneath our Pn ray paths (Schaeffer and Lebedev, 2013). We

extracted values of vertically polarized tomographic shear velocity anomaly ($\%dV_s$) at 100 km intervals along each ray path, from slices through the SL2013sv model at depths of 25, 50, 75 and 150 km. We then calculated the mean $\%dV_s$ along each ray path, at each depth interval (Figure 8). At 25 and 50 km depths, the effects of the ridge axis are evident, with higher velocities associated with ray paths travelling off-axis (detected by EA2 and EA8), and hence not sampling the relatively low-velocity axial region (Figures 8a and 8b). This effect is less pronounced at 75 km depth (Figure 8c), and is not apparent at 150 km depth, which presumably reflects sub-plate velocities. The lack of correlation between SL2013sv and P_n velocities at 150 km suggests that our V_{P_n} estimates, sensitive to the velocity structure directly beneath the Moho, do not record deeper, larger-scale sub-plate (i.e. asthenospheric) processes and anomalies. Hence our observed V_{P_n} variability may instead arise due to local variations in melt supply, lithospheric thickness, or faulting.

Conclusions

We used a network of five autonomous hydrophones and a broadband seismograph to detect P_n arrivals from regional earthquakes in the equatorial Atlantic Ocean over a period of ~12 months between 2012 and 2013. Our estimates of upper-mantle velocity from the travel times of 152 P_n arrivals broadly agree (mostly within 0.2 km s^{-1}) with those from nearby seismic refraction experiments.

We find that the upper-mantle near the St. Paul transform system has consistently high velocities ($>8 \text{ km s}^{-1}$), compared to relatively low velocities ($\sim 7.5 \text{ km s}^{-1}$) in the adjacent MAR spreading segments northwest of the transform. This spatial pattern is consistent with the notion that P_n ray paths sample lower velocity mantle near the ridge axis, and higher velocity material

near transforms, which are generally cooler, despite the presence of intra-transform spreading segments. We do not resolve any dependence between V_{Pn} and azimuth, which could either be due to observational uncertainty, or due to the combined effects of thickened lithosphere and more complex mantle upwelling patterns under slow-spreading conditions. We also do not find any correlation between V_{Pn} and vertically polarized shear speed from the global SL2013sv model, indicating that our method is not sensitive to properties of the asthenosphere. The close agreement between our results and those from seismic refraction experiments demonstrates that the relatively simple method of using sparse arrays of autonomous hydrophones to detect Pn arrivals can be used to obtain accurate estimates of upper-mantle velocities. Hence, this method provides a useful complement to deployments of other seafloor instruments such as ocean bottom seismographs, in remote areas where direct observations are typically elusive.

Data and Resources

All Pn velocities obtained in this study using the hydrophones data of the COLMEIA/EA array (Smith *et al.*, 2012; Maia *et al.*, 2014) and the seismic records of the and ASPSP station (de Melo and do Nascimento., 2018), are presented in tables of Supplemental Material. Analysis and figure preparation were carried out using the Generic Mapping Tools version 5.4.5 (Wessel *et al.*, 2013), Seismic Analysis Code (Helffrich *et al.*, 2013). Earthquake locations used in this work were obtained from the International Seismological Center Bulletin database at www.isc.ac.uk/iscbulletin/search/bulletin/ (last accessed November 2019). The Global Centroid Moment Tensor Project database of Ekström *et al.* (2012) was searched using www.globalcmt.org/CMTsearch.html (last accessed November 2019).

367

368

369 **Acknowledgements**

370 This research was supported by National Science Foundation grants EAR-1062238, EAR-
371 1062165 and OCE-1839727, and by an InterRidge Student Fellowship for GWSdM. The
372 COLMEIA expedition was funded by the French Ministry of Research through its grant to the
373 French Oceanographic Fleet. COLMEIA hydrophone deployment was funded by LABEX MER
374 grant “Actions à la mer”, and instruments were recovered with the help of the Brazilian Navy.
375 AFdN thanks the support of the Brazilian Navy and CNPq for grants 392484441/2012-4 and
376 303817/2014-3. This paper is NOAA/Pacific Marine Environmental Laboratory contribution
377 number 5116. We thank Associate Editor, T. Brocher, B. VanderBeek, and an anonymous
378 reviewer for their constructive input. Any opinion, findings, and conclusions or
379 recommendations expressed in this material are those of the authors and do not necessarily
380 reflect the views of the National Science Foundation.

381

References

- Abercrombie, R. E., and G. Ekstrom (2001). Earthquake slip on oceanic transform faults, *Nature* **410**, 74–77.
- Barlow, J. (2019). Global Ocean Sound Speed Profile Library (GOSSPL), an Rdata resource for studies of ocean sound propagation, *NOAA Tech. Memo. NMFS SWFSC* **612**, no. March, 1–7, doi: 10.25923/7DJ1-J540.
- Bondár, I., and D. Storchak (2011). Improved location procedures at the International Seismological Centre, *Geophys. J. Int.* **186**, no. 3, 1220–1244, doi: 10.1111/j.1365-246X.2011.05107.x.
- Brandsdottir, B., and W. Menke (1997). Faroe-Iceland Ridge Experiment, 2, Crustal structure of the Krafla central volcano, *J. Geophys. Res.* **102**, no. B4, 7867–7886.
- Campos, T., F. H. R. Bezerra, N. K. Srivastava, M. M. Vieira, and C. Vita-Finzi (2010). Holocene tectonic uplift of the St Peter and St Paul Rocks (Equatorial Atlantic) consistent with emplacement by extrusion, *Mar. Geol.* **271**, no. 1–2, 177–186, doi: 10.1016/j.margeo.2010.02.013.
- Canales, J. P., J. A. Collins, and R. S. Detrick (2000). Seismic structure across the rift valley of the Mid-Atlantic Ridge at 23°20' (MARK area): Implications for crustal accretion processes at slow spreading ridges, *J. Geophys. Res.* **105**, no. B12, 28411–28425, doi: 10.1029/2000JB900301.
- Christeson, G. L., J. A. Goff, and R. S. Reece (2019). Synthesis of Oceanic Crustal Structure From Two-Dimensional Seismic Profiles, *Rev. Geophys.* **57**, doi: 10.1029/2019RG000641.
- Chulick, G. S., S. Detweiler, and W. D. Mooney (2013). Seismic structure of the crust and uppermost mantle of South America and surrounding oceanic basins, *J. South Am. Earth*

Sci. **42**, 260–276, doi: 10.1016/j.jsames.2012.06.002.

Chulick, G. S., and W. D. Mooney (2002). Seismic Structure of the Crust and Uppermost Mantle of North America and Adjacent Oceanic Basins: A Synthesis, *Bull. Seismol. Soc. Am.* **92**, no. 6, 2478–2492, doi: 10.1016/j.jsames.2012.06.002.

D’Eu, J. F., J. Y. Royer, and J. Perrot (2012). Long-term autonomous hydrophones for large-scale hydroacoustic monitoring of the oceans, in *Proceedings of Oceans, 2012-Yeosu*, IEEE, 1–6, doi: 10.1109/OCEANS-Yeosu.2012.6263519.

de Melo, G., and A. F. do Nascimento (2018). Earthquake Magnitude Relationships for the Saint Peter and Saint Paul Archipelago, Equatorial Atlantic, *Pure Appl. Geophys.* **175**, no. 3, 741–756, doi: 10.1007/s00024-017-1732-6.

DeMets, C., R. G. Gordon, and D. F. Argus (2010). Geologically current plate motions, *Geophys. J. Int.* **181**, 1–80, doi: 10.1111/j.1365-246X.2009.04491.x.

Dunn, R. A., V. Lekić, R. S. Detrick, and D. R. Toomey (2005). Three-dimensional seismic structure of the Mid-Atlantic Ridge (35°N): Evidence for focused melt supply and lower crustal dike injection, *J. Geophys. Res. Solid Earth* **110**, no. 9, 1–17, doi: 10.1029/2004JB003473.

Dziak, R. P., D. R. Bohnenstiehl, H. Matsumoto, C. G. Fox, D. K. Smith, M. Tolstoy, T. K. Lau, J. H. Haxel, and M. J. Fowler (2004). P- and T-wave detection thresholds, Pn velocity estimate, and detection of lower mantle and core P-waves on ocean sound-channel hydrophones at the Mid-Atlantic Ridge, *Bull. Seism. Soc. Am.* **94**, no. 2, 665–677, doi: 10.1785/0120030156.

Dziewonski, A. M., and D. L. Anderson (1981). Preliminary reference Earth model, *Phys. Earth Planet. Inter.* **25**, 297–356.

- Ekström, G., M. Nettles, and A. M. Dziewoński (2012). The global CMT project 2004-2010: Centroid-moment tensors for 13,017 earthquakes, *Phys. Earth Planet. Inter.* **200–201**, 1–9, doi: 10.1016/j.pepi.2012.04.002.
- Fox, C. G., H. Matsumoto, and T.-K. A. Lau (2001). Monitoring Pacific Ocean seismicity from an autonomous hydrophone array, *J. Geophys. Res.* **106**, no. 10, 41834206, doi: 10.1029/2000JB900404.
- Francis, T. J. G., I. T. Porter, and R. C. Lilwall (1978). Microearthquakes near the eastern end of St Paul's fracture zone, *Geophys. J. R. Astron. Soc.* **53**Reprint, 201–217.
- Gaherty, J. B., D. Lizarralde, J. A. Collins, G. Hirth, and S. Kim (2004). Mantle deformation during slow seafloor spreading constrained by observations of seismic anisotropy in the western Atlantic, *Earth Planet. Sci. Lett.* **228**, no. 3–4, 255–265, doi: 10.1016/j.epsl.2004.10.026.
- Gasperini, L., G. Carrara Marco Ligi, P. Fabretti, D. Brunelli, A. Cipriani, S. Susini, and P. Tartarotti (1997). New data on the geology of the Romanche FZ., equatorial Atlantic: PRIMAR-96 cruise report, **3**, no. 59, 1–2.
- Growe, K., I. Grevenmeyer, S. Singh, and C. Papenberg (2019). Seismic structure of the St . Paul Fracture Zone near 18°W in the Atlantic Ocean – evidence for a magmatic origin of crust, *Geophys. Res. Abstr.* **21**, 4770.
- Helffrich, G., J. Wookey, and I. Bastow (2013). *The Seismic Analysis Code: A Primer and User's Guide*, Cambridge, UK.
- Hooft, E. E. E., R. S. Detrick, D. R. Toomey, J. A. Collins, and J. Lin (2000). Crustal thickness and structure along three contrasting spreading segments of the Mid-Atlantic Ridge, 33.5°–35°N, *J. Geophys. Res. Solid Earth* **105**, no. B4, 8205–8226, doi: 10.1029/1999jb900442.

- Kennett, B. L. N., and E. R. Engdahl (1991). Traveltimes for global earthquake location and phase identification, *Geophys. J. Int.* **105**, no. 2, 429–465, doi: 10.1111/j.1365-246X.1991.tb06724.x.
- Le Pichon, X., R. E. Houtz, C. L. Drake, and J. E. Nafe (1965). Crustal structure of the mid-ocean ridges: 1. Seismic refraction measurements, *J. Geophys. Res.* **70**, no. 2, 319–339, doi: 10.1029/jz070i002p00319.
- Lin, P. Y. P., J. B. Gaherty, G. Jin, J. A. Collins, D. Lizarralde, R. L. Evans, and G. Hirth (2016). High-resolution seismic constraints on flow dynamics in the oceanic asthenosphere, *Nature* **535**, no. 7613, 538–541, doi: 10.1038/nature18012.
- Lin, J., and J. Phipps Morgan (1992). The spreading rate dependence of three-dimensional mid-ocean ridge gravity structure, *Geophys. Res. Lett.* **19**, no. 1, 13–16.
- Linehan, D. (1940). Earthquakes in the West Indian region, *Eos Trans. AGU* **21**, no. 2, 229–232, doi: doi:10.1029/TR021i002p00229.
- Lohman, R. B., and M. Simons (2005). Locations of selected small earthquakes in the Zagros mountains, *Geochemistry, Geophys. Geosystems* **6**, no. 3, doi: 10.1029/2004GC000849.
- Maia, M., I. Brehme, U. F. Fluminense, A. Briaïs, and D. Brunelli (2014). Preliminary report on the COLMEIA Cruise, Equatorial Atlantic Recife, January 24 - Recife, February 28, 2013, *InterRidge News* **22**, 52–56, doi: 10.1029/2005JB004210.Von.
- Maia, M., S. Sichel, A. Briaïs, D. Brunelli, M. Ligi, N. Ferreira, T. Campos, B. Mougél, I. Brehme, C. Hémond, *et al.* (2016). Extreme mantle uplift and exhumation along a transpressive transform fault, *Nat. Geosci.* **9**, no. 8, 619–623, doi: 10.1038/ngeo2759.
- Mark, H. F., D. Lizarralde, J. A. Collins, N. C. Miller, G. Hirth, J. B. Gaherty, and R. L. Evans (2019). Azimuthal Seismic Anisotropy of 70-Ma Pacific-Plate Upper Mantle, *J. Geophys.*

Res. Solid Earth **124**, no. 2, 1889–1909, doi: 10.1029/2018JB016451.

Müller, R. D., M. Sdrolias, C. Gaina, and W. R. Roest (2008). Age, spreading rates, and spreading asymmetry of the world's ocean crust, *Geochem. Geophys. Geosyst* **9**, no. 4, 1–19, doi: 10.1029/2007GC001743.

Nicolas, A., and N. I. Christensen (2011). Formation of anisotropy in upper mantle peridotites - A review, in *Composition, structure and dynamics of the lithosphere-asthenosphere system, Geodynamics* K. Fuchs, and C. Froidevaux(Editors), American Geophysical Union, Washington, D. C., 111–123, doi: 10.1029/gd016p0111.

Raitt, R. W., J. Shor, G. G., T. J. G. Francis, and G. B. Morris (1969). Anisotropy of the Pacific upper mantle, *J. Geophys. Res.* **74**, no. 12, 3095–3109, doi: <https://doi.org/10.1029/JB074i012p03095>.

Ribe, N. M. (1989). Seismic anisotropy and mantle flow, *J. Geophys. Res.* **94**, no. B4, 4213–4223, doi: 10.1029/JB094iB04p04213.

Schaeffer, A. J., and S. Lebedev (2013). Global shear speed structure of the upper mantle and transition zone, *Geophys. J. Int.* **194**, no. 1, 417–449, doi: 10.1093/gji/ggt095.

Sleep, N. H. (1975). Formation of Oceanic Crust: Some Thermal Constraints, *J. Geophys. Res.* **80**, no. 29, 4037–4042.

Smith, D. K., R. P. Dziak, C. Palmiotto, R. Parnell-Turner, and A. Zheleznov (2012). The seismicity of the equatorial Mid-Atlantic Ridge and its long-offset transforms, *Abstr. OS13B-1720 Present. 2012 Fall Meet. AGU, San Fr. Calif. 5-9 Dec.*

Taylor, J. (1997). *Introduction to Error Analysis, the Study of Uncertainties in Physical Measurements*, University Science Books, New York, NY.

Turcotte, D. L., and G. Schubert (2002). *Geodynamics*, Cambridge University Press, doi:

10.1017/CBO9780511807442.

- Udintsev, G. B., H. J., V. G. Udintsev, and A. B. Knjazev (1996). Topography of the Equatorial Segment of the Mid-Atlantic Ridge After Multi-Beam Echo-sounding., in *Equatorial Segment of the Mid-Atlantic Ridge: IOC Technical Series No. 46* G. B. Udintsev(Editor), United Nations Educational, Scientific and Cultural Organization, Paris, France, 8–15.
- VanderBeek, B. P., and D. R. Toomey (2017). Shallow Mantle Anisotropy Beneath the Juan de Fuca Plate, *Geophys. Res. Lett.* **44**, no. 22, 11,382–11,389, doi: 10.1002/2017GL074769.
- Wessel, P., W. H. F. Smith, R. Scharoo, J. Luis, and F. Wobbe (2013). Generic Mapping Tools: Improved Version Released, *Eos Trans. AGU* **94**, no. 45, 409–410.
- Weston, J., A. M. G. Ferreira, and G. J. Funning (2012). Systematic comparisons of earthquake source models determined using InSAR and seismic data, *Tectonophysics* **532–535**, 61–81, doi: 10.1016/j.tecto.2012.02.001.
- Zhang, Z., and S. Karato (1995). Lattice preferred orientation of olivine aggregates in simple shear, *Nature* **375**, 774–777.

512 **Author mailing addresses**

513

514 Departamento de Geofísica, Federal University of Rio Grande do Norte, Natal, Brazil

515 (GWSdM, AFN), gwsmelo@ufrn.edu.br

516 Institute of Geophysics and Planetary Physics, Scripps Institution of Oceanography, University

517 of California, San Diego, CA, USA

518 (RPT)

519 NOAA, Pacific Marine Environmental Laboratory, Newport, OR, USA

520 (RPD)

521

522 National Science Foundation, Alexandria, VA, USA

523 (DKS)

524

525 Laboratoire Geosciences Ocean, CNRS and University of Brest

526 LGO-IUEM, rue Dumont Durville, 29280 Plouzane, France

527 (MM and JYR)

528

529

530

Table 1. Details of seismograph (S) and hydrophone (H) sensors used for Pn analysis. Sensor depth is given below sea level (bsl); water delay is based upon cable length, and water/crust corrections are applied to each Pn ray path individually.

Station name	Sensor type	Lat, °N	Lon, °E	Depth bsl, m	Cable length, m	Water delay, s	Crust path correction, km	Crust travel time correction, s
ASPSP	S	0.9169	-29.3459	-16	-	-	12.5	1.9
EA2	H	4.9907	-22.9931	800	3912	2.10	23.8	7.2
EA8	H	-2.5159	-29.2181	800	3242	2.54	23.0	6.5
H2	H	1.3297	-31.3445	700	2260	1.57	21.8	5.5
H4	H	0.4123	-24.6437	700	1860	1.24	21.3	5
H5	H	0.1552	-27.7875	700	3060	2.04	22.8	6.3

Figures

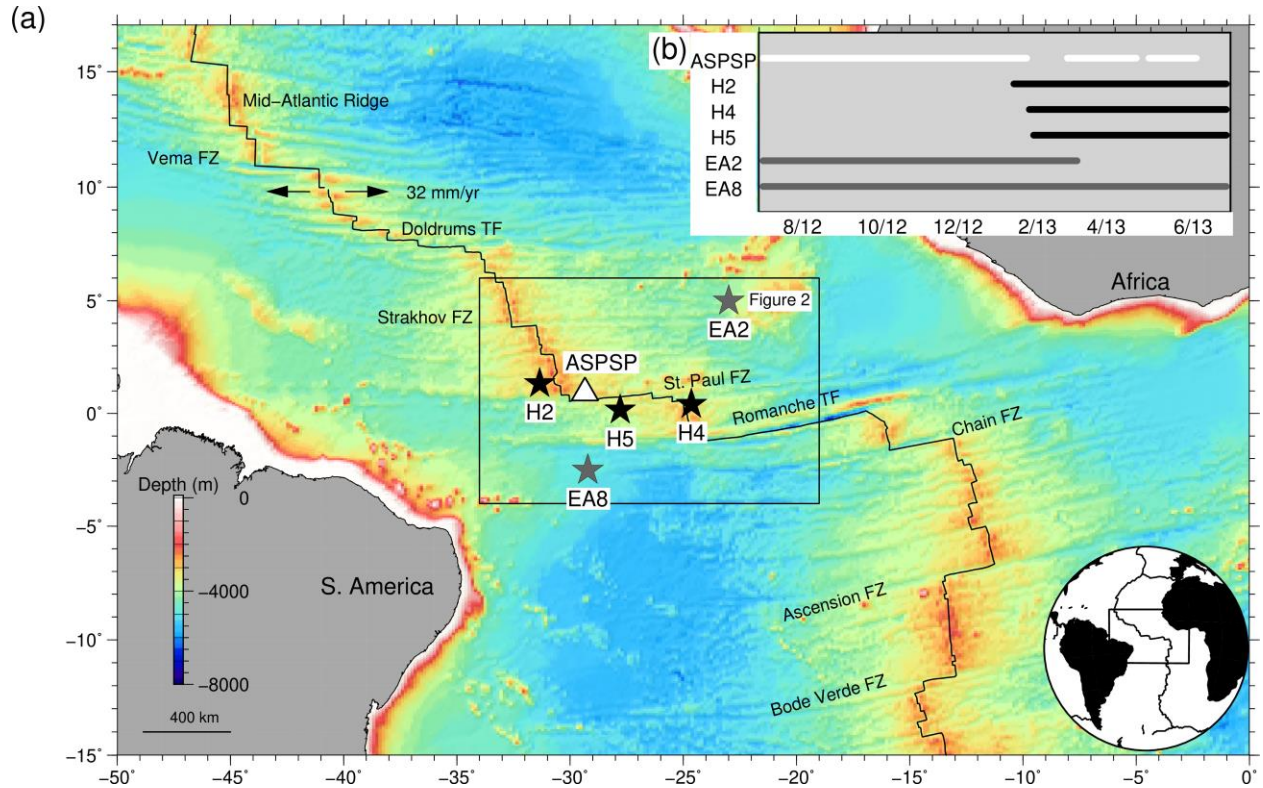


Figure 1. a) Regional bathymetric map of equatorial Atlantic ocean. White triangle shows ASPSP seismograph station, located on St. Peter and St. Paul islets; black/gray stars are COLMEIA / EA hydrophone networks, respectively (Smith *et al.*, 2012; Maia *et al.*, 2014); black line is Mid-Atlantic Ridge, with selected transforms and half-spreading rate noted (arrows). Black box shows location of Figure 2. **b)** Bars show instrument recording intervals: ASPSP (white), COLMEIA (black), and EA (gray).

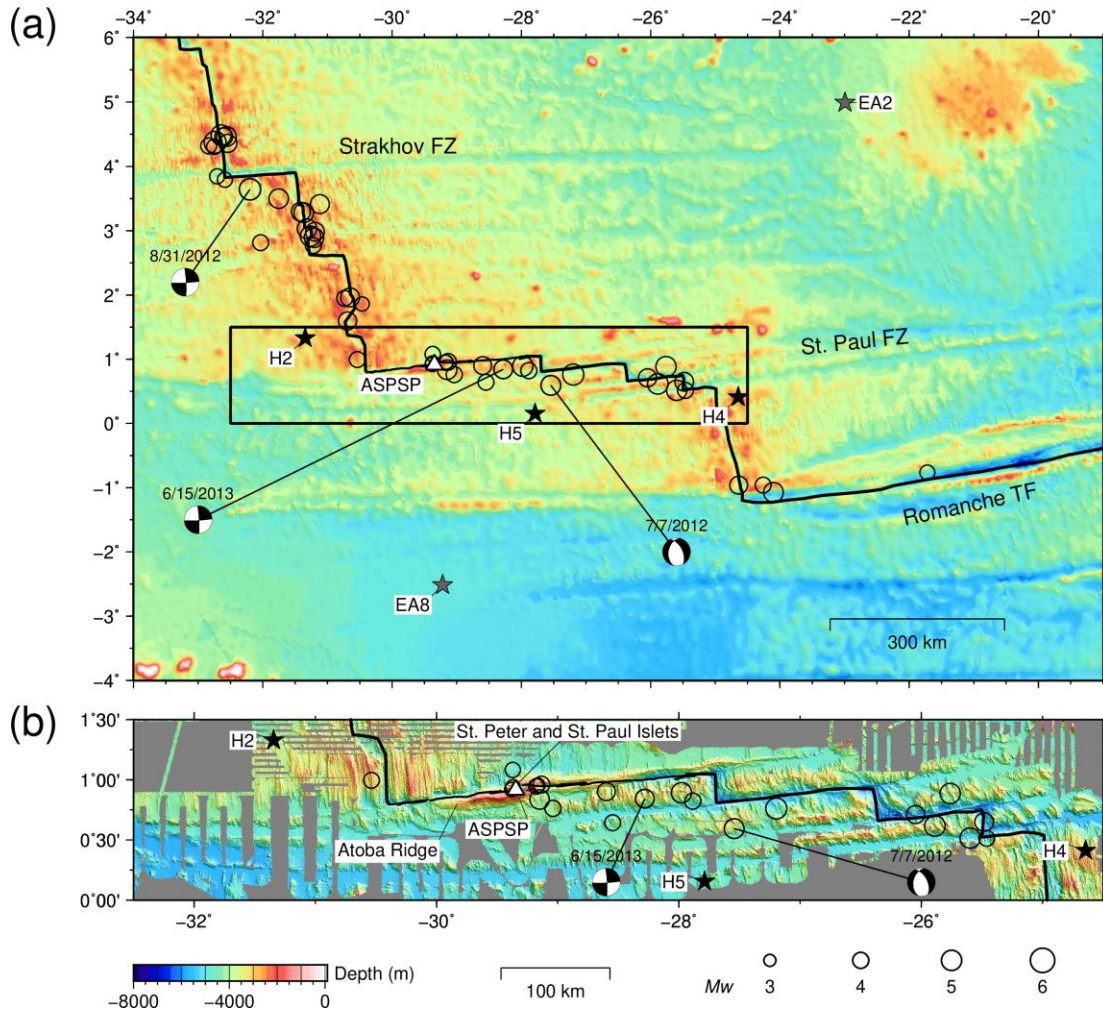


Figure 2. a) Bathymetric map of equatorial Atlantic ocean. Black box shows location of (b).

Circles are earthquakes used in Pn analysis, scaled by M_w ; triangle shows ASPSP

station; black/gray stars are COLMEIA / EA hydrophone networks, respectively (Smith *et al.*,

2012; Maia *et al.*, 2014); black line is Mid-Atlantic Ridge, with selected transforms labeled;

beach-balls are centroid moment tensors for three exemplar earthquakes (Ekström *et al.*, 2012),

waveforms shown in Figures 4 and 5. **b)** Bathymetric map showing details of St. Peter and St.

Paul fracture zone (from Udintsev *et al.*, 1996; Gasperini *et al.*, 1997; Maia *et al.*, 2016).

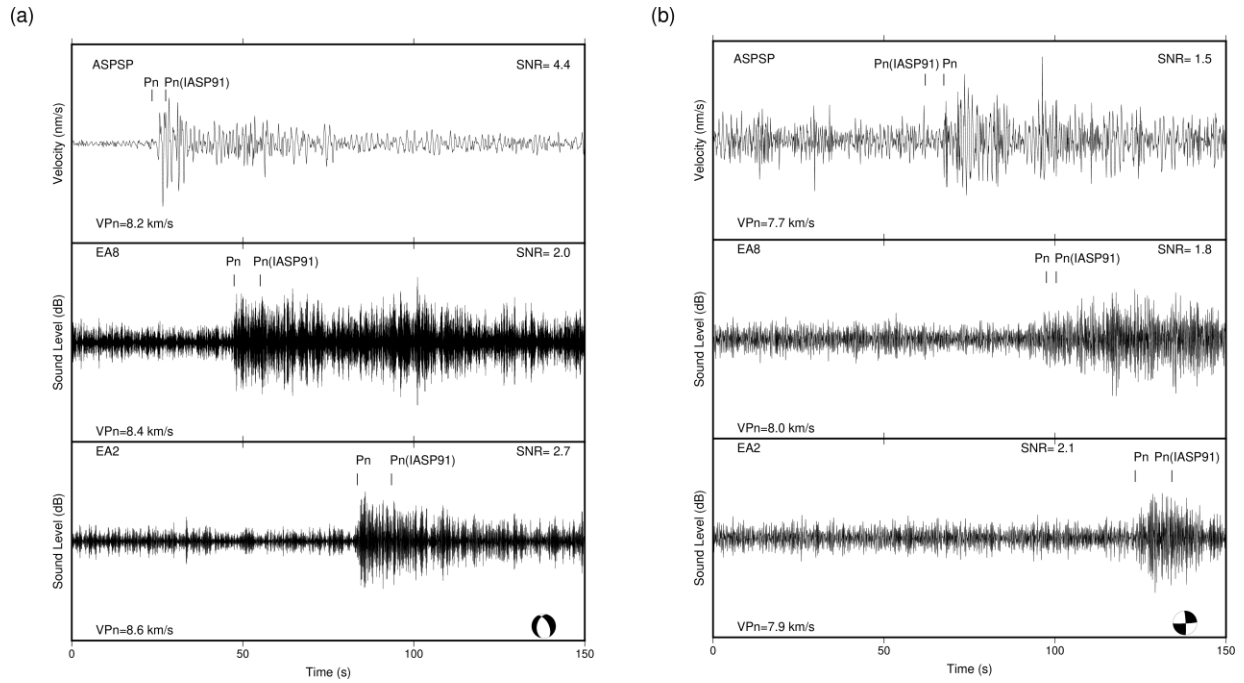


Figure 3. Example waveforms recorded by the ASPSP seismograph and EA array hydrophones, with 4–12 Hz and 6–20 Hz Butterworth filters applied, respectively. **a)** M_w 4.9 normal faulting event on 7th July 2012, located on the St. Paul transform fault at 27.5°W. Picked P_n arrivals, and P_n arrivals predicted by iasp91 model are marked; beach-balls are centroid moment tensors (Ekström et al., 2012); V_{Pn} and signal to noise ratio (SNR) noted for each station (this study), SNR calculated STA/LTA. **b)** M_w 5.3 strike-slip event on 31st August 2012, located on Strakhov transform fault near 32.5°W.

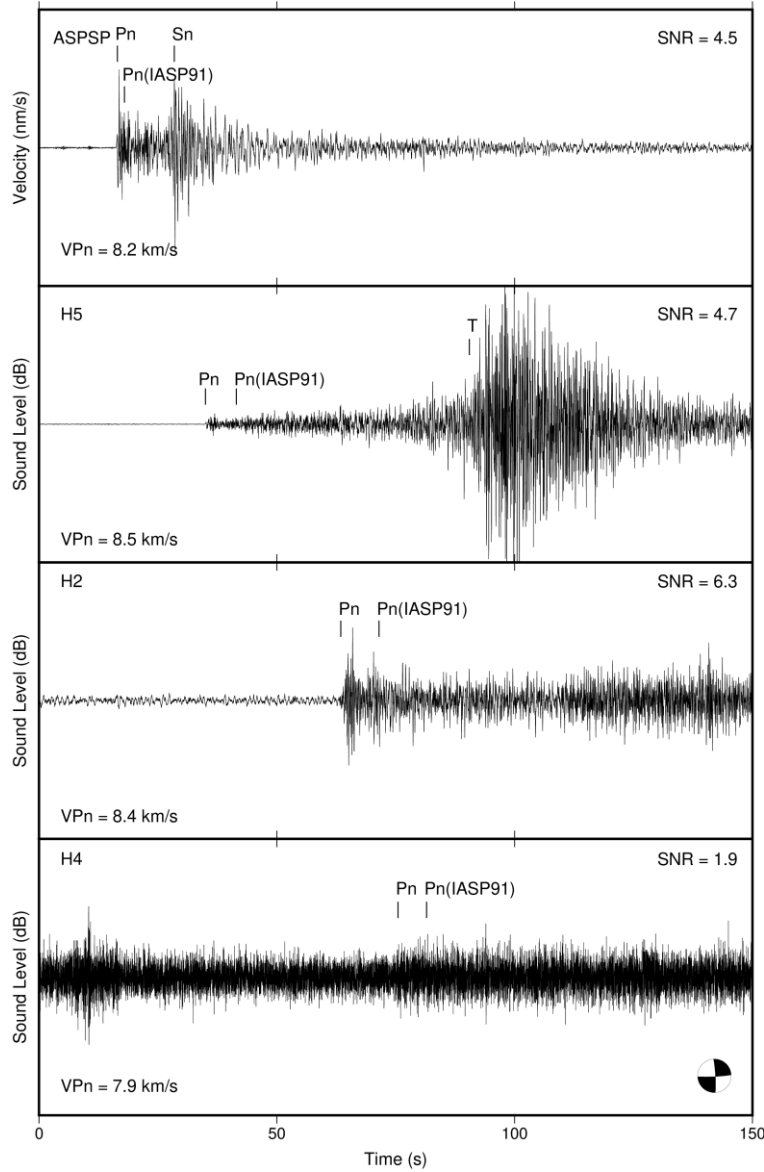


Figure 4. Example of waveforms recorded by the ASPSP seismograph and COLMEIA hydrophones, with 4–12 Hz and 6–20 Hz Butterworth filters applied, respectively, for mb 4.6 strike-slip event on 15th June 2013, located near St. Paul transform fault at 29.5°W. Picked *Pn* arrivals, and *Pn* arrivals predicted by iasp91 model are marked; beach-balls are centroid moment tensors (Ekström et al., 2012); V_{Pn} and SNR noted for each station (this study).

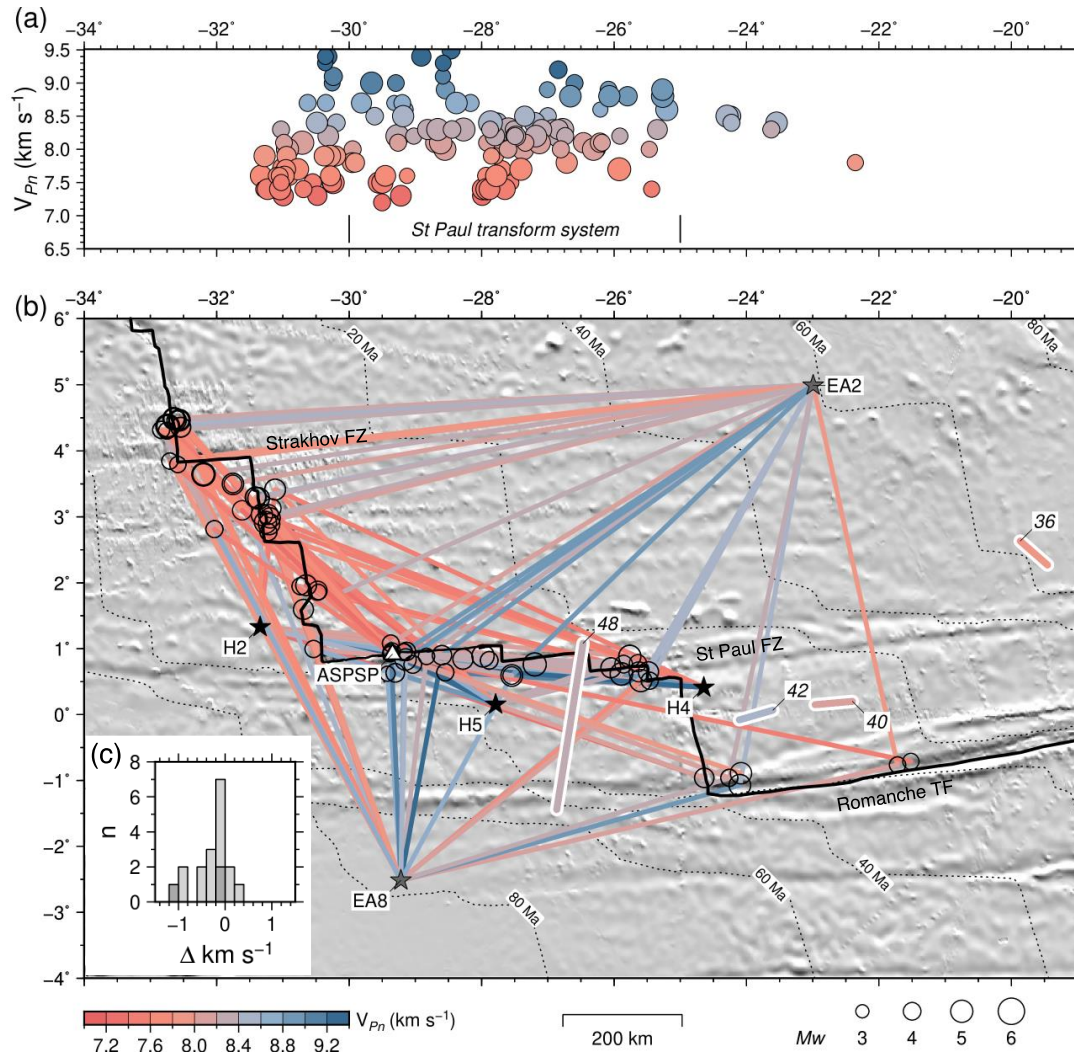
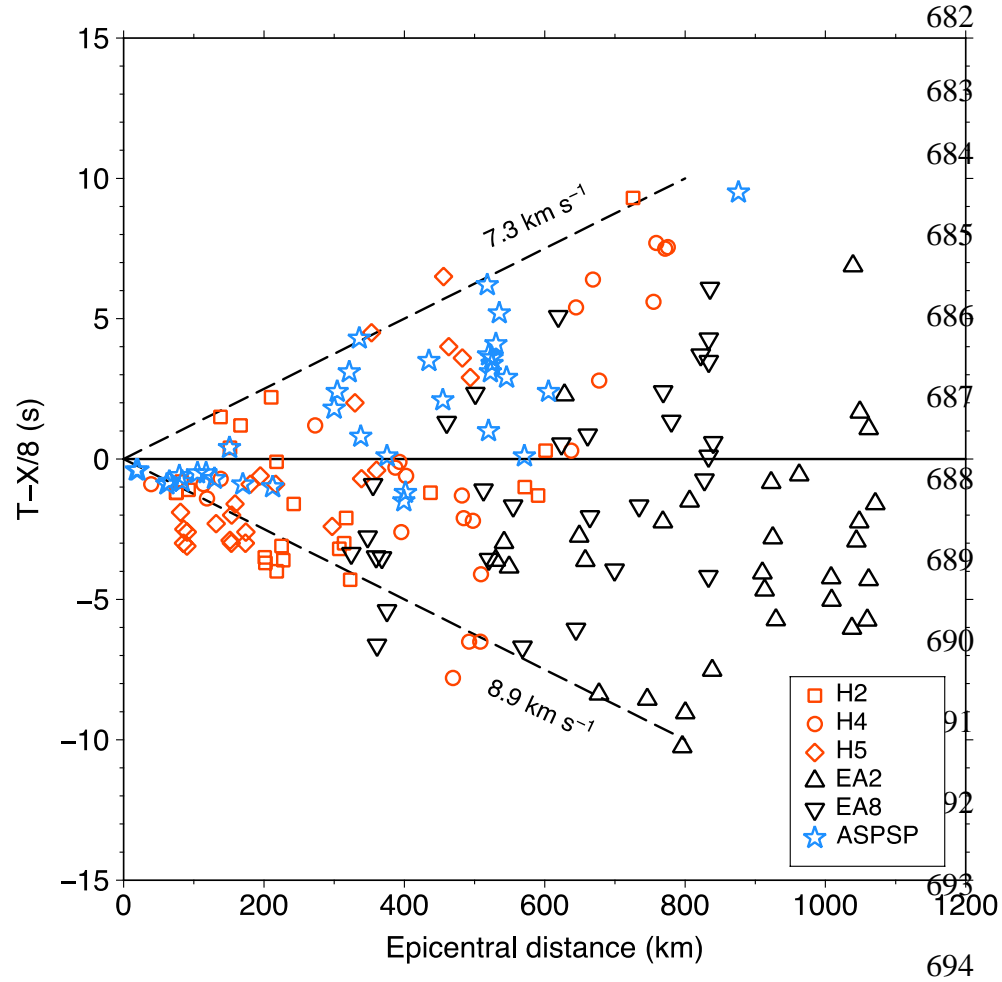


Figure 5. a) V_{Pn} plotted against mean longitude of ray path. Circle radius scaled by magnitude of source event; colored by V_{Pn} ; St. Paul transform system marked by vertical bars. **b)** Shaded relief map showing stations, earthquakes, and ray paths. Circles are earthquakes used in Pn analysis, scaled by M_w ; colored lines are ray paths shaded by Pn velocity; white triangle is ASPSP station; black/gray stars are COLMEIA / EA hydrophone networks, respectively; thick lines numbered 48, 42, 40, and 36 are seismic refraction profiles from cruise AT40-180 (Le Pichon *et al.*, 1965), shaded by velocity; dotted lines are isochrons, modified from Müller *et al.* (2008) to remove artifacts associated with fracture zone traces. **c)** Histogram of difference

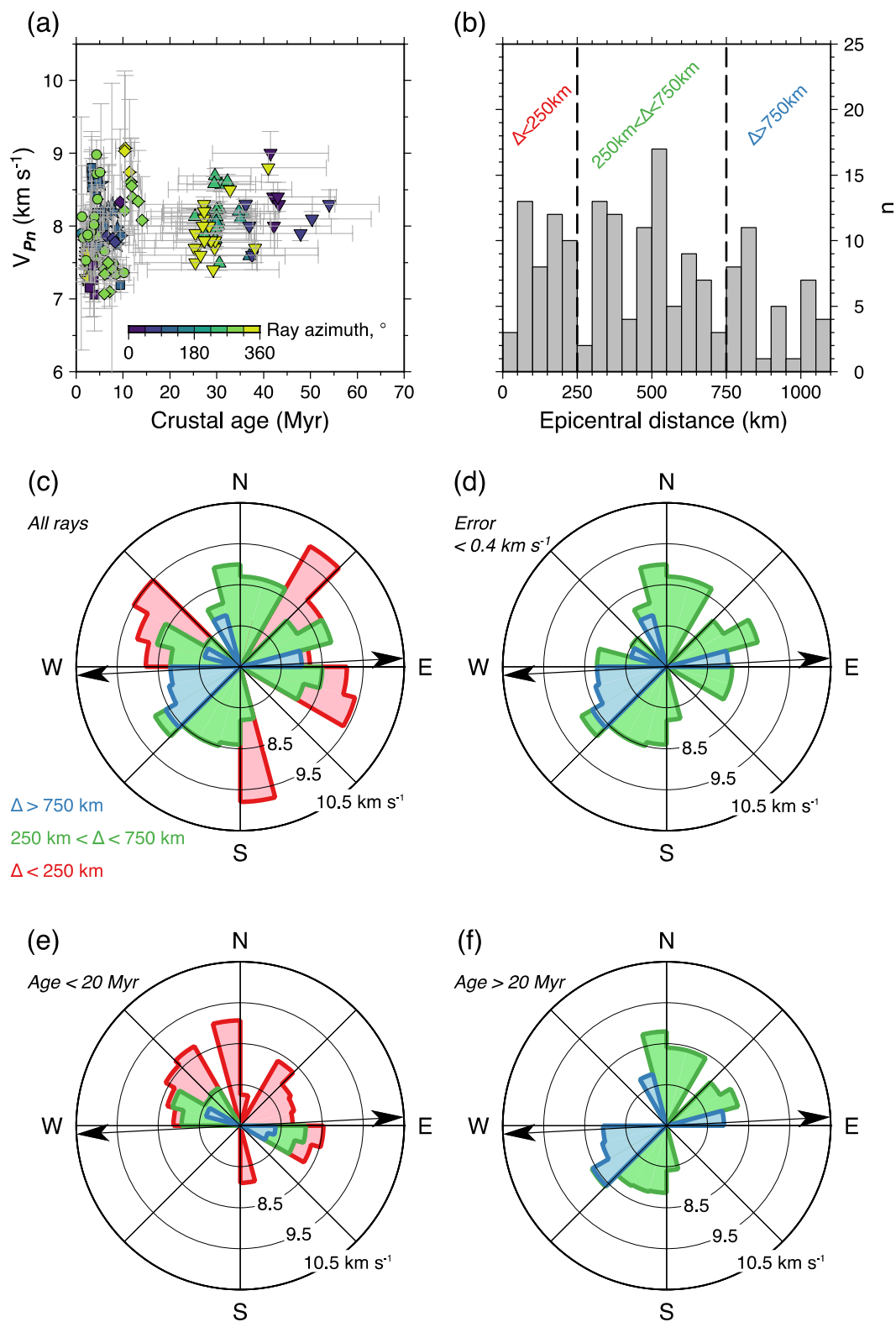
678 between velocity estimates from refraction experiment (Le Pichon *et al.*, 1965), and intersecting
679 ray paths from this study; positive values indicate higher velocities estimated by refraction
680 experiment; dark/light gray bars are velocities from profiles AT40-180 48 and 42, respectively.
681



695

696 **Figure 6.** Reduced travel time versus epicentral distance, plotted with a reduction velocity of 8
 697 km s^{-1} , approximately corresponding to velocity immediately below Moho from PREM and
 698 iasp91 models (solid line; Dziewonski and Anderson, 1981; Kennett and Engdahl, 1991); dashed
 699 lines show velocity bounds of 7.3 and 8.9 km s^{-1} ; key shows recording station symbols.

700



701

702

Figure 7. a) V_{Pn} plotted against oceanic crustal age at epicentral location, colored by ray azimuth (crustal ages assigned from model of Müller *et al.*, 2008); key for station symbols given in Figure 6; horizontal error bars are 2σ crustal age along ray path, vertical error bars are V_{Pn} uncertainty described in text. **b)** Histogram of epicentral distances; dotted lines show cut-offs used to define categories in anisotropy analysis. **c)** Sector diagram showing V_{Pn} vs. azimuth for all rays; length of sectors scaled by median V_{Pn} , calculated in 15° bins, and colored by epicentral distance category; black arrows show plate spreading vector. **d)** Median V_{Pn} vs. azimuth for rays with V_{Pn} uncertainty $< 0.4 \text{ km s}^{-1}$, colored by epicentral distance category. **e)** Median V_{Pn} vs. azimuth for rays sampling crust $< 20 \text{ Myr}$ in age, colored by epicentral distance category. **f)** Median V_{Pn} vs. azimuth for rays sampling crust $> 20 \text{ Myr}$ in age, colored by epicentral distance category.

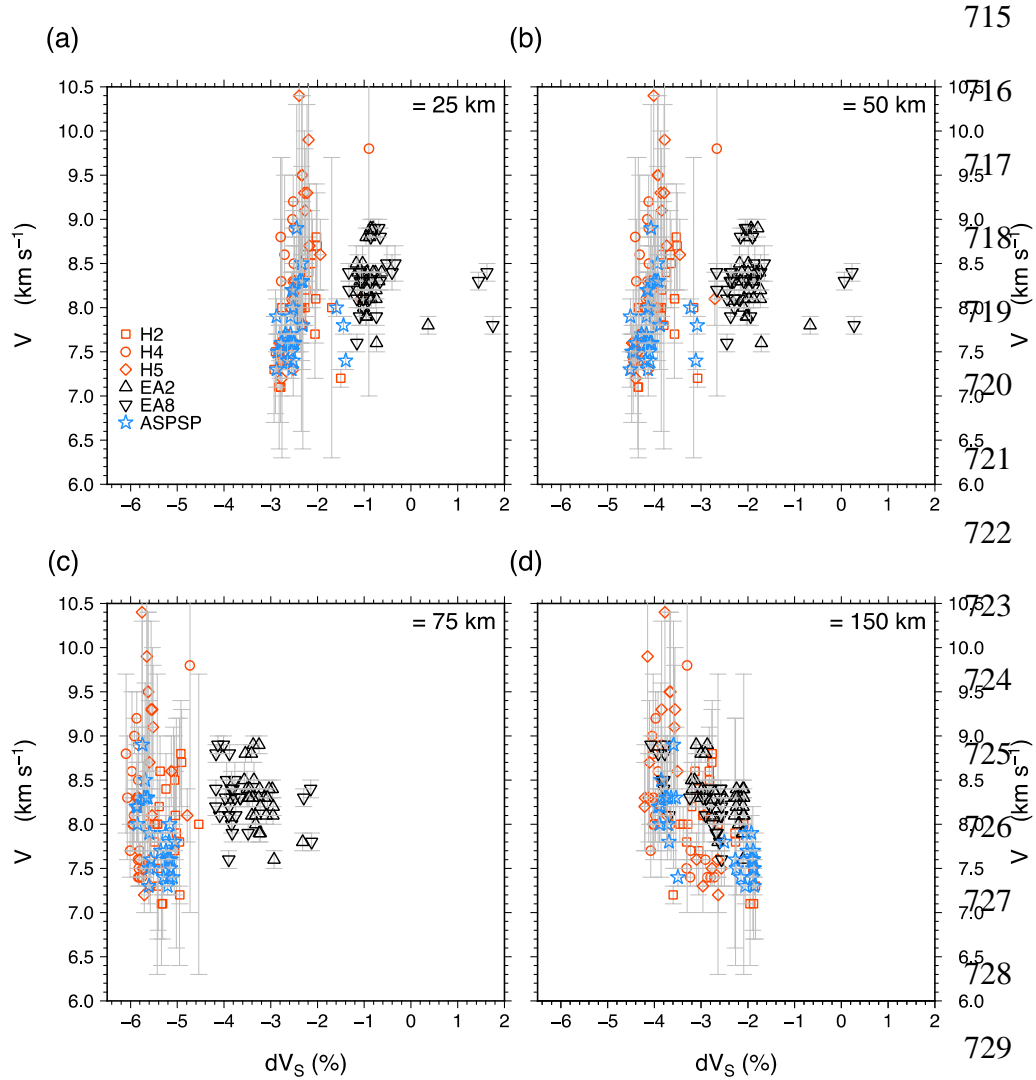


Figure 8. (a-d) Relationship between V_{Pn} and vertically polarized tomographic shear velocity anomaly at depths of 25, 50, 75 and 150 km, respectively, from global model SL2013sv (Schaeffer and Lebedev, 2013).

Supplemental Material for: Uppermost mantle velocity beneath the Mid-Atlantic Ridge and transform faults in the equatorial Atlantic ocean

Guilherme W. S. de Melo, Ross Parnell-Turner, Robert P. Dziak, Deborah K. Smith, Marcia Maia, Aderson F. do Nascimento, and Jean-Yves Royer

Description of the Supplemental Material

This supplemental material consists of one table, seven figures, accompanying narrative text and related references, and one Excel spreadsheet.

Supplemental Text

Table S1 provides the catalog of 50 earthquakes used in P_n velocity analysis, and the Table S2 contains the parameters used for V_{P_n} estimates from individual source-receiver pairs. Figures S1 to S6 show common-receiver record sections for each station used in the study, which aid the identification of P_n phases in the waveform data. As documented elsewhere, P_n arrivals are often emergent and noisy (e.g. VanderBeek and Toomey, 2017), and hence difficult to identify when plotted as record sections, in particular when using data recorded by moored hydrophones. We also note that microseism noise obscures P_n arrivals recorded by the station ASPSP at epicentral distances > 350 km, due to this station being located on the St. Peter and St. Paul islets (de Queiroz *et al.*, 2017). Figure S7 shows estimates of the signal to noise ratio (SNR), calculated for all arrivals, and used to illustrate uncertainties in arrival time picks.

Supplemental Tables

Table S1. Catalog of 50 earthquakes used in Pn velocity analysis; magnitude estimates (de Melo and do Nascimento, 2018) hypocenters and origin times from ISC catalog. Note all depths are 10 km.

Table S2. V_{Pn} parameters for velocity estimate for each source-receiver pair, including origin times, hypocenter locations, Pn travel time, Pn distance, and Pn velocity estimates for the 50 earthquakes. They present the complete list of 152 raypaths.

Supplemental Figures

Figures S1. Common-receiver record section for seismograph ASPSP on St Peter and St Paul islets; waveforms plotted with a 4–12 Hz Butterworth filter, amplitudes scaled to minimize overlap between adjacent traces; dashed solid/dashed lines show range of likely Pn velocities; colored triangles are Pn arrival picks.

Figures S2. Common-receiver record sections for hydrophone H2; waveforms plotted with a 6–20 Hz Butterworth filter, amplitudes scaled to minimize overlap between adjacent traces; dashed solid/dashed lines show range of likely Pn velocities; colored triangles are Pn arrival picks.

Figures S3. Common-receiver record sections for hydrophone H4; waveforms plotted with a 6–20 Hz Butterworth filter; amplitudes scaled to minimize overlap between adjacent traces; dashed solid/dashed lines show range of likely Pn velocities; colored triangles are Pn arrival picks.

Figures S4. Common-receiver record section for hydrophone H5; waveforms plotted with a 6–20 Hz Butterworth filter, amplitudes scaled to minimize overlap between adjacent traces; dashed solid/dashed lines show range of likely Pn velocities; colored triangles are Pn arrival picks.

Figures S5. Common-receiver record section for hydrophone EA2; waveforms plotted with a 6–20 Hz Butterworth filter, amplitudes scaled to minimize overlap between adjacent traces; dashed solid/dashed lines show range of likely Pn velocities; colored triangles are Pn arrival picks.

Figures S6. Common-receiver record section for hydrophone EA8; waveforms plotted with a 6–20 Hz Butterworth filter, amplitudes scaled to minimize overlap between adjacent traces; dashed solid/dashed lines show range of likely Pn velocities; colored triangles are Pn arrival picks.

Figure S7. Noise characterization of Pn arrivals. **a)** Signal to noise ratio estimated from the ratio between short time (1 s window) and long time (20 s window) average amplitudes ($SNR_{STA/LTA}$), as a function of epicentral distance, key shows symbols used for stations. **b)** SNR estimated from ratio between the peak amplitude and the root mean square noise amplitude (SNR_{amp}), as a function of epicentral distance. **c)** $SNR_{STA/LTA}$ as a function of magnitude. **d)** SNR_{amp} as a function of magnitude. **e)** $SNR_{STA/LTA}$ vs. SNR_{amp} , symbols with error bars are mean values of SNR for each station ± 1 standard deviation.

Table S1. Catalog of 50 earthquakes used in *Pn* velocity analysis; magnitude estimates (de Melo and do Nascimento, 2018) hypocenters and origin times from ISC catalog. Note all depths are 10 km.

Event	Date	Origin time, UTC	Lat, ° N	Long, ° W	Mag, Mw
1	Jul. 07. 2012	15:11:45	0.594	27.544	4.9
2	Jul. 09. 2012	15:40:22	0.836	29.149	4.8
3	Jul. 11. 2012	10:48:11	-0.961	24.259	3.9
4	Jul. 13. 2012	10:00:13	2.814	32.034	3.9
5	Jul. 14. 2012	06:47:17	3.281	31.366	4.9
6	Jul. 17. 2012	09:21:50	2.917	31.263	5.0
7	Jul. 18. 2012	05:43:30	2.984	31.193	4.6
8	Jul. 28. 2012	15:20:17	3.845	32.707	3.7
9	Jul. 28. 2012	15:23:42	4.306	32.751	3.8
10	Jul. 28. 2012	16:01:11	4.375	32.738	5.4
11	Jul. 28. 2012	16:02:33	4.459	32.604	4.4
12	Jul. 28. 2012	16:03:59	4.319	32.839	3.9
13	Jul. 28. 2012	16:12:38	3.793	32.585	3.7
14	Jul. 28. 2012	16:18:46	4.488	32.642	5.0
15	Aug. 09. 2012	08:59:23	-1.072	24.099	4.9
16	Aug. 16. 2012	08:04:57	0.514	25.461	3.9
17	Aug. 18. 2012	16:02:47	0.946	29.176	3.8
18	Aug. 22. 2012	10:19:55	4.464	32.562	4.9
19	Aug. 23. 2012	05:14:32	1.082	29.371	3.8
20	Aug. 31. 2012	00:35:35	3.644	32.199	5.3
21	Aug. 31. 2012	03:52:29	3.5	31.753	4.8
22	Sep. 19. 2012	02:26:33	-0.764	21.719	3.7
23	Sep. 23. 2012	06:29:39	1.597	30.689	4.5
24	Sep. 24. 2012	00:55:51	0.516	25.596	5.0
25	Oct. 26. 2012	14:57:30	0.901	28.599	4.4
26	Oct. 31. 2012	15:13:12	4.359	32.541	4.5
27	Nov. 11. 2012	08:02:28	3.296	31.411	4.7
28	Dec. 03. 2012	11:03:19	0.649	25.481	4.6
29	Feb. 26. 2013	06:29:28	0.762	29.039	4.0
30	Mar. 24. 2013	16:23:43	0.616	25.888	5.1
31	Apr. 01. 2013	20:01:10	0.892	27.978	5.0
32	Apr. 01. 2013	20:03:00	0.823	27.885	4.0
33	Apr. 03. 2013	05:29:36	0.761	27.197	5.2
34	Apr. 08. 2013	20:33:41	0.643	28.547	3.9
35	Apr. 09. 2013	03:07:04	3.415	31.118	4.7
36	Apr. 09. 2013	03:46:45	2.892	31.208	4.8
37	Apr. 14. 2013	04:28:40	2.769	31.218	3.9
38	Apr. 26. 2013	11:06:45	0.711	26.047	4.5
39	May. 06. 2013	21:15:49	0.94	29.37	3.6
40	May. 07. 2013	08:21:09	0.92	29.38	3.5
41	May. 21. 2013	00:51:04	-0.96	24.638	4.4
42	May. 28. 2013	22:32:39	0.96	29.134	4.1
43	May. 31. 2013	10:19:26	0.886	25.762	5.0
44	Jun. 12. 2013	03:54:05	0.955	29.165	3.6
45	Jun. 15. 2013	20:37:31	0.843	28.281	4.6
46	Jul. 20. 2013	01:59:52	1.963	30.65	4.7
47	Jul. 20. 2013	12:32:49	0.996	30.537	3.9
48	Jul. 21. 2013	14:54:12	1.949	30.734	3.9
49	Jul. 25. 2013	05:13:50	1.86	30.462	3.5
50	Aug. 09. 2013	01:26:16	3.032	31.316	4.8

All depths of these earthquakes are 10 km in the ISC catalog.

Table S2. V_{Pn} parameters for velocity estimate for each source-receiver pair, including origin times, hypocenter locations, Pn travel time, Pn distance, and Pn velocity estimates for the 50 earthquakes. They present the complete list of 152 raypaths.

Station	Date (ISC)	Origin Time (ISC)	Lat (ISC)	Lon (ISC)	Depth km (ISC)	Mag (ISC)	Great Circle Distance km	Pn Distance km	Travel Time. s	Pn Travel Time. s	Total error. km/s	VPn. km/s
EA2	2012-07-07	15:11:45	0.59390	-27.5438	10.0	4.9	701.2	677.4	83.5	76.3	0.1	8.9
EA8	2012-07-07	15:11:45	0.59390	-27.5438	10.0	4.9	391.1	368.1	49.0	42.5	0.3	8.7
ASPSP	2012-07-07	15:11:45	0.59390	-27.5440	10.0	4.0	183.6	170.0	22.4	20.4	0.5	8.3
EA2	2012-07-09	15:40:22	0.83630	-29.1490	10.0	4.8	824.2	800.4	98.2	91.0	0.1	8.8
EA8	2012-07-09	15:40:22	0.83630	-29.1490	10.0	4.8	370.8	347.8	47.2	40.7	0.3	8.5
ASPSP	2012-07-11	10:48:11	-0.96100	-24.2591	10.0	3.9	584.7	571.1	73.5	71.5	0.1	8.0
EA2	2012-07-11	10:48:11	-0.96100	-24.2591	10.0	3.9	673.0	649.2	85.6	78.4	0.1	8.3
EA8	2012-07-11	10:48:11	-0.96100	-24.2591	10.0	3.9	577.9	554.9	74.2	67.7	0.2	8.2
EA2	2012-07-13	10:00:13	2.81410	-32.0339	10.0	3.9	1032.0	1008.2	129.0	121.8	0.1	8.3
EA8	2012-07-13	10:00:13	2.81410	-32.0339	10.0	3.9	667.5	644.5	81.0	74.5	0.1	8.7
ASPSP	2012-07-13	10:00:13	2.81410	-32.0339	10.0	3.9	335.1	321.5	45.3	43.3	0.2	7.4
EA2	2012-07-14	06:47:17	3.28140	-31.3666	10.0	4.9	948.7	924.9	120.0	112.8	0.1	8.2
EA8	2012-07-14	06:47:17	3.28140	-31.3666	10.0	4.9	684.2	661.2	90.0	83.5	0.1	7.9
ASPSP	2012-07-14	06:47:17	3.28140	-31.3666	10.0	4.4	349.2	335.6	48.2	46.2	0.2	7.3
EA2	2012-07-17	09:21:50	2.91710	-31.2627	10.0	5.0	946.5	922.7	121.7	114.5	0.1	8.1
EA8	2012-07-17	09:21:50	2.91710	-31.2627	10.0	5.0	642.4	619.4	89.0	82.5	0.1	7.5
ASPSP	2012-07-17	09:21:50	2.91710	-31.2627	10.0	4.5	313.6	300.0	41.3	39.3	0.3	7.6
EA2	2012-07-18	05:43:30	2.98460	-31.1929	10.0	4.6	937.2	913.4	116.7	109.5	0.1	8.3
EA8	2012-07-18	05:43:30	2.98460	-31.1929	10.0	4.6	646.7	623.7	85.0	78.5	0.1	7.9
ASPSP	2012-07-18	05:43:30	2.98460	-31.1929	10.0	4.3	318.0	304.4	42.5	40.5	0.3	7.5
EA2	2012-07-28	15:20:17	3.84550	-32.7071	10.0	3.7	1085.6	1061.8	141.0	133.8	0.1	7.9
EA8	2012-07-28	15:20:17	3.84550	-32.7071	10.0	3.7	803.4	780.4	105.4	98.9	0.1	7.9

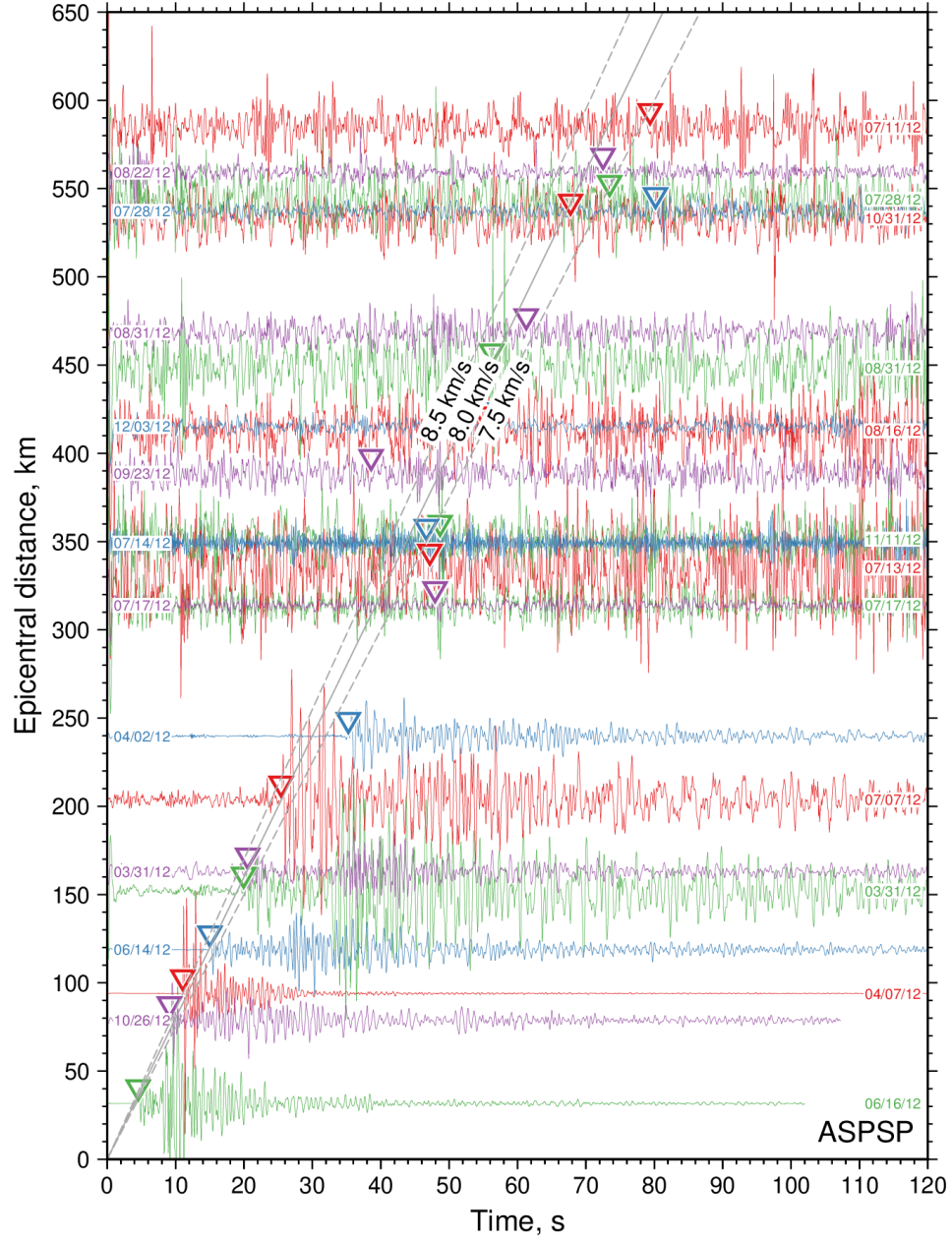
ASPSP	2012-07-28	15:20:17	3.84550	-32.7071	10.0	3.7	544.1	530.5	72.4	70.4	0.1	7.5
ASPSP	2012-07-28	15:23:42	4.30570	-32.7514	10.0	3.8	538.6	525.0	71.2	69.2	0.1	7.6
EA2	2012-07-28	15:23:42	4.30570	-32.7514	10.0	3.8	1085.4	1061.6	135.6	128.4	0.1	8.3
EA8	2012-07-28	15:23:42	4.30570	-32.7514	10.0	3.8	850.6	827.6	109.2	102.7	0.1	8.1
ASPSP	2012-07-28	16:01:11	4.37560	-32.7379	10.0	4.8	548.9	535.3	74.1	72.1	0.1	7.4
EA2	2012-07-28	16:01:11	4.37560	-32.7379	10.0	5.4	1083.3	1059.5	133.9	126.7	0.1	8.4
EA8	2012-07-28	16:01:11	4.37560	-32.7379	10.0	5.4	856.7	833.7	115.0	108.5	0.1	7.7
ASPSP	2012-07-28	16:02:33	4.45970	-32.6045	10.0	4.4	533.7	520.1	70.7	68.7	0.1	7.6
EA2	2012-07-28	16:02:33	4.45970	-32.6045	10.0	4.4	1067.9	1044.1	134.8	127.6	0.1	8.2
EA8	2012-07-28	16:02:33	4.45970	-32.6045	10.0	4.4	858.4	835.4	117.0	110.5	0.1	7.6
EA2	2012-07-28	16:03:59	4.31910	-32.8387	10.0	3.9	1094.9	1071.1	139.5	132.3	0.1	8.1
EA8	2012-07-28	16:03:59	4.31910	-32.8387	10.0	3.9	856.4	833.4	106.5	100.0	0.1	8.3
ASPSP	2012-07-28	16:03:59	4.31910	-32.8387	10.0	3.9	538.6	525.0	71.0	69.0	0.1	7.6
EA2	2012-07-28	16:12:38	3.79280	-32.5852	10.0	3.7	1072.9	1049.1	140.0	132.8	0.1	7.9
EA8	2012-07-28	16:12:38	3.79280	-32.5852	10.0	3.7	791.8	768.8	105.0	98.5	0.1	7.8
ASPSP	2012-07-28	16:12:38	3.79280	-32.5852	10.0	3.7	536.3	522.7	70.5	68.5	0.1	7.6
EA2	2012-07-28	16:18:46	4.48820	-32.6422	10.0	5.0	1071.9	1048.1	136.0	128.8	0.1	8.1
EA8	2012-07-28	16:18:46	4.48820	-32.6422	10.0	5.0	863.1	840.1	112.1	105.6	0.1	8.0
ASPSP	2012-07-28	16:18:46	4.48820	-32.6422	10.0	4.6	531.8	518.2	73.0	71.0	0.1	7.3
ASPSP	2012-08-09	08:59:23	-1.07230	-24.0997	10.0	4.8	618.9	605.3	80.1	78.1	0.1	7.8
EA2	2012-08-09	08:59:23	-1.07230	-24.0997	10.0	4.9	681.6	657.8	85.8	78.6	0.1	8.4
EA8	2012-08-09	08:59:23	-1.07230	-24.0997	10.0	4.9	591.4	568.4	70.9	64.4	0.2	8.8
EA2	2012-08-16	08:04:57	0.51390	-25.4608	10.0	3.9	566.0	542.2	72.0	64.8	0.2	8.4
EA8	2012-08-16	08:04:57	0.51390	-25.4608	10.0	3.9	535.8	512.8	69.5	63.0	0.2	8.1
ASPSP	2012-08-16	08:04:57	0.51390	-25.4608	10.0	3.9	412.9	399.3	50.4	48.4	0.2	8.2
EA2	2012-08-18	16:02:47	0.94600	-29.1760	10.0	3.8	819.9	796.1	96.5	89.3	0.1	8.9
EA8	2012-08-18	16:02:47	0.94600	-29.1760	10.0	3.8	382.8	359.8	48.0	41.5	0.3	8.7
ASPSP	2012-08-22	10:19:55	4.46400	-32.5619	10.0	4.4	559.3	545.7	73.1	71.1	0.1	7.7
EA2	2012-08-22	10:19:55	4.46400	-32.5619	10.0	4.9	1063.2	1039.4	144.0	136.8	0.1	7.6
EA8	2012-08-22	10:19:55	4.46400	-32.5619	10.0	4.9	856.8	833.8	114.2	107.7	0.1	7.7
EA2	2012-08-23	05:14:32	1.08200	-29.3710	10.0	3.8	830.2	806.4	106.5	99.3	0.1	8.1

EA8	2012-08-23	05:14:32	1.08200	-29.3710	10.0	3.8	398.2	375.2	48.0	41.5	0.3	9.0
EA2	2012-08-31	00:35:35	3.64410	-32.1987	10.0	5.3	1032.6	1008.8	128.3	121.1	0.1	8.3
EA8	2012-08-31	00:35:35	3.64410	-32.1987	10.0	5.3	757.6	734.6	96.7	90.2	0.1	8.1
ASPSP	2012-08-31	00:35:35	3.64410	-32.1987	10.0	4.8	468.5	454.9	61.0	59.0	0.2	7.7
EA2	2012-08-31	03:52:29	3.50060	-31.7535	10.0	4.8	986.4	962.6	127.0	119.8	0.1	8.0
EA8	2012-08-31	03:52:29	3.50060	-31.7535	10.0	4.8	722.6	699.6	90.0	83.5	0.1	8.4
ASPSP	2012-08-31	03:52:29	3.50060	-31.7535	10.0	4.0	448.6	435.0	59.9	57.9	0.2	7.5
EA2	2012-09-19	02:26:33	-0.76440	-21.7191	10.0	3.7	652.0	628.2	88.0	80.8	0.1	7.8
EA8	2012-09-19	02:26:33	-0.76440	-21.7191	10.0	3.7	856.6	833.6	110.8	104.3	0.1	8.0
ASPSP	2012-09-19	02:26:33	-0.71000	-21.5190	10.0	3.7	889.6	876.0	121.0	119.0	0.1	7.4
EA2	2012-09-23	06:22:39	1.59680	-30.6888	10.0	4.5	933.9	910.1	116.9	109.7	0.1	8.3
EA8	2012-09-23	06:22:39	1.59680	-30.6888	10.0	4.5	483.3	460.3	65.4	58.9	0.2	7.8
ASPSP	2012-09-23	06:22:39	1.59680	-30.6888	10.0	4.3	164.6	151.0	21.3	19.3	0.5	7.8
ASPSP	2012-09-24	00:55:51	0.51650	-25.5963	10.0	4.0	388.8	375.2	49.0	47.0	0.2	8.0
EA2	2012-09-24	00:55:51	0.51650	-25.5963	10.0	5.0	573.2	549.4	72.0	64.8	0.2	8.5
EA8	2012-09-24	00:55:51	0.51650	-25.5963	10.0	5.0	524.3	501.3	71.5	65.0	0.2	7.7
EA2	2012-10-26	14:57:30	0.90120	-28.5988	10.0	4.4	769.9	746.1	91.9	84.7	0.1	8.8
EA8	2012-10-26	14:57:30	0.90120	-28.5988	10.0	4.4	384.0	361.0	45.0	38.5	0.3	9.4
ASPSP	2012-10-26	14:57:30	0.90120	-28.5988	10.0	4.4	78.7	65.1	9.3	7.3	1.4	8.9
ASPSP	2012-10-31	15:13:12	4.35950	-32.5410	10.0	4.4	533.4	519.8	68.0	66.0	0.2	7.9
EA2	2012-10-31	15:13:12	4.35950	-32.5410	10.0	4.5	1061.6	1037.8	130.9	123.7	0.1	8.4
EA8	2012-10-31	15:13:12	4.35950	-32.5410	10.0	4.5	845.4	822.4	113.0	106.5	0.1	7.7
ASPSP	2012-11-11	08:02:28	3.29600	-31.4112	10.0	4.5	351.4	337.8	45.0	43.0	0.2	7.9
EA2	2012-11-11	08:02:28	3.29600	-31.4112	10.0	4.7	953.2	929.4	117.7	110.5	0.1	8.4
EA8	2012-11-11	08:02:28	3.29600	-31.4112	10.0	4.7	687.4	664.4	87.5	81.0	0.1	8.2
ASPSP	2012-12-03	11:03:19	0.64900	-25.6250	10.0	4.5	415.2	401.6	51.0	49.0	0.2	8.2
EA2	2012-12-03	11:03:19	0.64940	-25.4813	10.0	4.6	554.0	530.2	69.9	62.7	0.2	8.5
EA8	2012-12-03	11:03:19	0.64940	-25.4813	10.0	4.6	543.6	520.6	68.0	61.5	0.2	8.5
H2	2013-02-26	06:29:28	0.76200	-29.0390	10.0	4.0	264.2	242.4	34.2	28.7	0.5	8.4
H4	2013-02-26	06:29:28	0.76200	-29.0390	10.0	4.0	490.8	469.5	55.9	50.9	0.3	9.2
H5	2013-02-26	06:29:28	0.76200	-29.0390	10.0	4.0	154.6	131.8	20.5	14.2	1.0	9.3

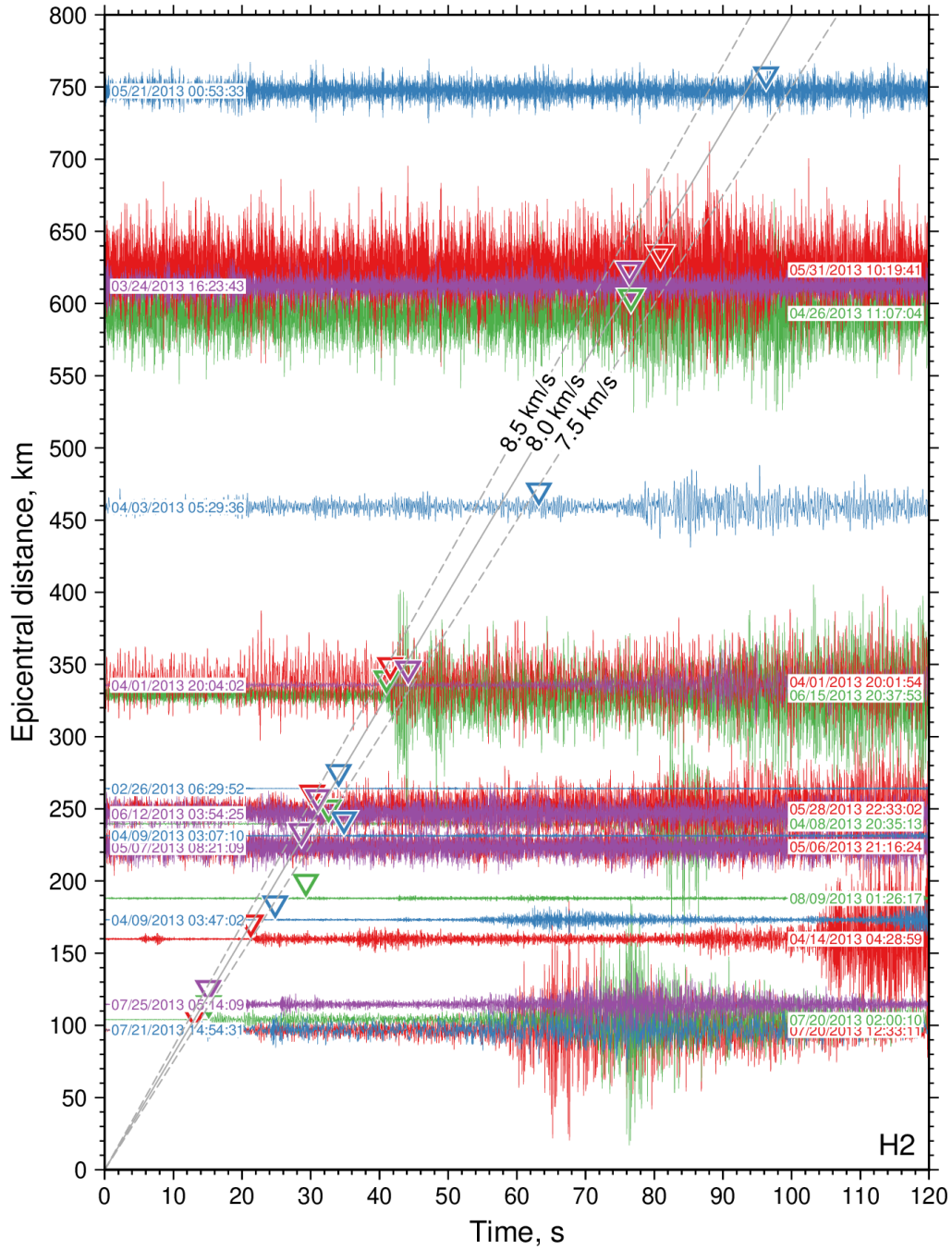
H2	2013-03-24	16:23:43	0.61600	-25.8880	10.0	5.1	612.4	590.6	78.0	72.5	0.2	8.1
H4	2013-03-24	16:23:43	0.61600	-25.8880	10.0	5.1	140.3	119.0	18.5	13.5	0.9	8.8
H5	2013-03-24	16:23:43	0.61600	-25.8880	10.0	5.1	217.5	194.7	30.0	23.7	0.5	8.2
ASPSP	2013-04-01	20:01:10	0.89200	-27.9790	10.0	5.0	131.0	117.4	16.2	14.2	0.7	8.3
H2	2013-04-01	20:01:10	0.89170	-27.9786	10.0	5.0	344.5	322.7	41.5	36.0	0.4	9.0
H4	2013-04-01	20:01:10	0.89170	-27.9786	10.0	5.0	408.5	387.2	53.1	48.1	0.3	8.0
H5	2013-04-01	20:01:10	0.89200	-27.9790	10.0	5.0	108.0	85.2	14.0	7.7	1.9	11.1
ASPSP	2013-04-01	20:03:00	0.82300	-27.8850	10.0	4.0	143.0	129.4	17.5	15.5	0.7	8.3
H2	2013-04-01	20:03:00	0.82300	-27.8850	10.0	4.0	338.8	317.0	43.0	37.5	0.3	8.5
H4	2013-04-01	20:03:00	0.82300	-27.8850	10.0	4.0	414.3	393.0	54.0	49.0	0.3	8.0
H5	2013-04-01	20:03:00	0.82300	-27.8850	10.0	4.0	113.0	90.2	14.5	8.2	1.8	11.0
ASPSP	2013-04-03	05:29:36	0.76100	-27.1970	10.0	5.2	226.0	212.4	27.6	25.6	0.4	8.3
H2	2013-04-03	05:29:36	0.76100	-27.1970	10.0	5.2	459.2	437.4	59.0	53.5	0.2	8.2
H4	2013-04-03	05:29:36	0.76100	-27.1970	10.0	5.2	294.2	272.9	40.3	35.3	0.3	7.7
H5	2013-04-03	05:29:36	0.91000	-27.1970	10.0	5.2	103.8	81.0	14.5	8.2	1.7	9.9
ASPSP	2013-04-08	20:33:41	0.64300	-28.5470	10.0	3.9	93.0	79.4	11.3	9.3	1.1	8.5
H2	2013-04-08	20:33:41	0.64300	-28.5470	10.0	3.9	239.6	217.8	32.6	27.1	0.5	8.0
H4	2013-04-08	20:33:41	0.64300	-28.5470	10.0	3.9	513.6	492.3	60.0	55.0	0.2	9.0
H5	2013-04-08	20:33:41	0.64300	-28.5470	10.0	3.9	181.5	158.7	24.5	18.2	0.7	8.7
H2	2013-04-09	03:07:04	3.41500	-31.1180	10.0	4.7	231.9	210.1	34.0	28.5	0.4	7.4
H4	2013-04-09	03:07:04	3.41500	-31.1180	10.0	4.7	793.0	771.7	109.0	104.0	0.1	7.4
H5	2013-04-09	03:07:04	3.41500	-31.1180	10.0	4.7	516.9	494.1	71.0	64.7	0.2	7.6
H2	2013-04-09	03:46:45	2.89200	-31.2080	10.0	4.8	173.4	151.6	24.8	19.3	0.7	7.9
H4	2013-04-09	03:46:45	2.89200	-31.2080	10.0	4.8	780.1	758.8	107.5	102.5	0.1	7.4
H5	2013-04-09	03:46:45	2.89200	-31.2080	10.0	4.8	486.2	463.4	68.3	62.0	0.2	7.5
H2	2013-04-14	04:28:40	2.76900	-31.2180	10.0	3.9	159.8	138.0	24.2	18.7	0.7	7.4
H4	2013-04-14	04:28:40	2.76900	-31.2180	10.0	3.9	776.6	755.3	105.0	100.0	0.1	7.6
H5	2013-04-14	04:28:40	2.76900	-31.2180	10.0	3.9	478.8	456.0	69.8	63.5	0.2	7.2
H2	2013-04-26	11:06:45	0.71100	-26.0470	10.0	4.5	593.6	571.8	76.0	70.5	0.2	8.1
H4	2013-04-26	11:06:45	0.71100	-26.0470	10.0	4.5	159.7	138.4	21.6	16.6	0.7	8.3
H5	2013-04-26	11:06:45	0.71100	-26.0470	10.0	4.5	203.2	180.4	28.0	21.7	0.6	8.3

H2	2013-05-06	21:15:49	0.94000	-29.3700	10.0	3.6	223.7	201.9	27.0	21.5	0.6	9.4
H4	2013-05-06	21:15:49	0.94000	-29.3700	10.0	3.6	529.6	508.3	62.0	57.0	0.2	8.9
H5	2013-05-06	21:15:49	0.94000	-29.3700	10.0	3.6	196.4	173.6	25.0	18.7	0.7	9.3
H2	2013-05-07	08:21:09	0.92000	-29.3800	10.0	3.5	222.9	201.1	27.1	21.6	0.6	9.3
H4	2013-05-07	08:21:09	0.92000	-29.3800	10.0	3.5	530.6	509.3	64.6	59.6	0.2	8.5
H5	2013-05-07	08:21:09	0.92000	-29.3800	10.0	3.5	196.9	174.1	25.5	19.2	0.7	9.1
H2	2013-05-21	00:51:04	-0.96000	-24.6380	10.0	4.4	747.5	725.7	105.5	100.0	0.1	7.3
H4	2013-05-21	00:51:04	-0.96000	-24.6380	10.0	4.4	60.5	39.2	9.0	4.0	2.8	9.8
H5	2013-05-21	00:51:04	-0.96000	-24.6380	10.0	4.4	361.7	338.9	48.0	41.7	0.3	8.1
H2	2013-05-28	22:32:39	0.96000	-29.1340	10.0	4.1	249.4	227.6	30.4	24.9	0.5	9.1
H4	2013-05-28	22:32:39	0.96000	-29.1340	10.0	4.1	503.5	482.2	64.0	59.0	0.2	8.2
H5	2013-05-28	22:32:39	0.96000	-29.1340	10.0	4.1	174.3	151.5	22.3	16.0	0.9	9.5
H2	2013-05-31	10:19:26	0.88600	-25.7620	10.0	5.0	623.2	601.4	81.0	75.5	0.2	8.0
H4	2013-05-31	10:19:26	0.88600	-25.7620	10.0	5.0	135.1	113.8	18.3	13.3	0.9	8.6
H5	2013-05-31	10:19:26	0.88600	-25.7620	10.0	5.0	239.5	216.7	32.5	26.2	0.5	8.3
H2	2013-06-12	03:54:05	0.95500	-29.1650	10.0	3.6	246.8	225.0	30.5	25.0	0.5	9.0
H4	2013-06-12	03:54:05	0.95500	-29.1650	10.0	3.6	506.1	484.8	63.5	58.5	0.2	8.3
H5	2013-06-12	03:54:05	0.95500	-29.1650	10.0	3.6	176.2	153.4	22.5	16.2	0.9	9.5
ASPSP	2013-06-15	20:37:31	0.84300	-28.2810	10.0	4.6	118.8	105.2	14.7	12.7	0.8	8.3
H2	2013-06-15	20:37:31	0.84300	-28.2810	10.0	4.6	329.1	307.3	40.7	35.2	0.4	8.7
H4	2013-06-15	20:37:31	0.84300	-28.2810	10.0	4.6	423.7	402.4	54.7	49.7	0.3	8.1
H5	2013-06-15	20:37:31	0.84300	-28.2810	10.0	4.6	113.3	90.5	15.0	8.7	1.7	10.4
H2	2013-07-20	01:59:52	1.96300	-30.6500	10.0	4.7	104.4	82.6	15.0	9.5	1.4	8.7
H4	2013-07-20	01:59:52	1.96300	-30.6500	10.0	4.7	690.1	668.8	95.0	90.0	0.1	7.4
H5	2013-07-20	01:59:52	1.96300	-30.6500	10.0	4.7	376.1	353.3	55.0	48.7	0.3	7.3
H2	2013-07-20	12:32:49	0.99600	-30.5370	10.0	3.9	97.1	75.3	13.7	8.2	1.7	9.2
H4	2013-07-20	12:32:49	0.99600	-30.5370	10.0	3.9	659.2	637.9	85.0	80.0	0.2	8.0
H5	2013-07-20	12:32:49	0.99600	-30.5370	10.0	3.9	319.9	297.1	41.0	34.7	0.4	8.6
H2	2013-07-21	14:54:12	1.94900	-30.7340	10.0	3.9	96.5	74.7	13.6	8.1	1.7	9.2
H4	2013-07-21	14:54:12	1.94900	-30.7340	10.0	3.9	698.8	677.5	92.5	87.5	0.1	7.7
H5	2013-07-21	14:54:12	1.94900	-30.7340	10.0	3.9	383.3	360.5	51.0	44.7	0.3	8.1

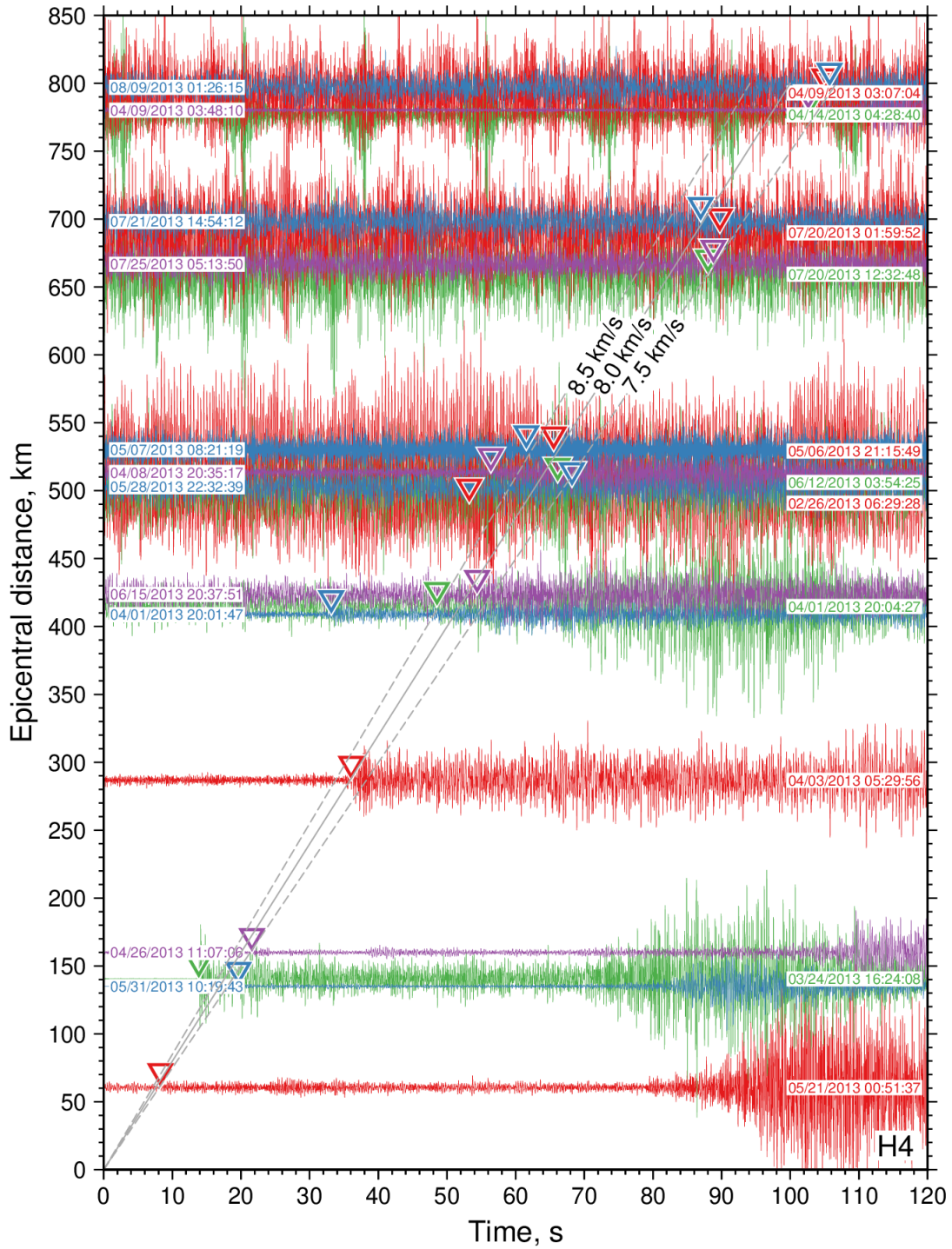
H2	2013-07-25	05:13:50	1.86000	-30.4620	10.0	3.5	114.4	92.6	16.0	10.5	1.3	8.8
H4	2013-07-25	05:13:50	1.86000	-30.4620	10.0	3.5	666.0	644.7	91.0	86.0	0.1	7.5
H5	2013-07-25	05:13:50	1.86000	-30.4620	10.0	3.5	352.3	329.5	49.5	43.2	0.3	7.6
H2	2013-08-09	01:26:16	3.03200	-31.3160	12.0	4.8	188.3	166.5	27.5	22.0	0.6	7.6
H4	2013-08-09	01:26:16	3.03200	-31.3160	12.0	4.8	796.9	775.6	109.5	104.5	0.1	7.4
H5	2013-08-09	01:26:16	3.03200	-31.3160	12.0	4.8	505.3	482.5	70.3	64.0	0.2	7.5



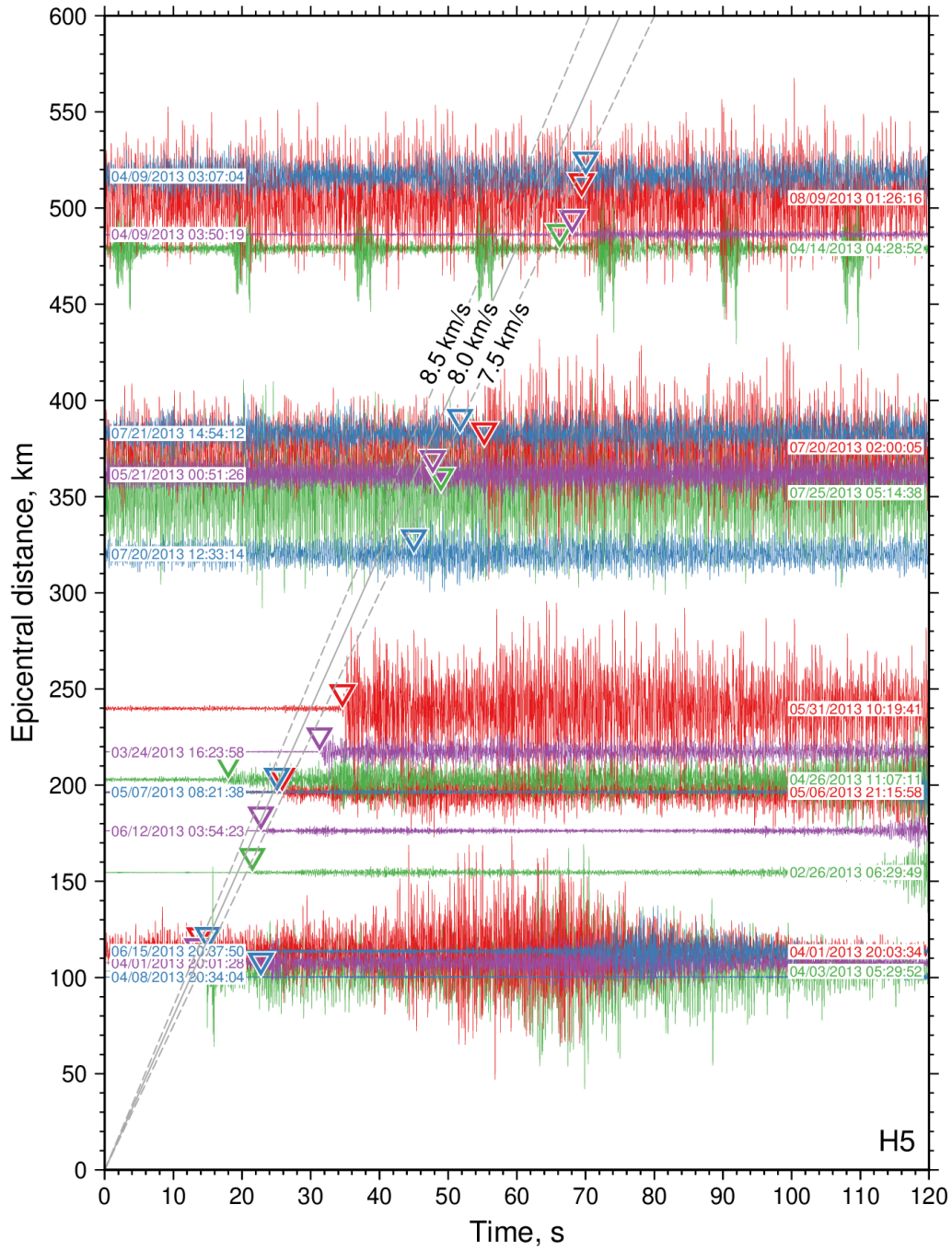
Figures S1. Common-receiver record section for seismograph ASPSP on St Peter and St Paul islets; waveforms plotted with a 4–12 Hz Butterworth filter, amplitudes scaled to minimize overlap between adjacent traces; dashed solid/dashed lines show range of likely *Pn* velocities; colored triangles are *Pn* arrival picks.



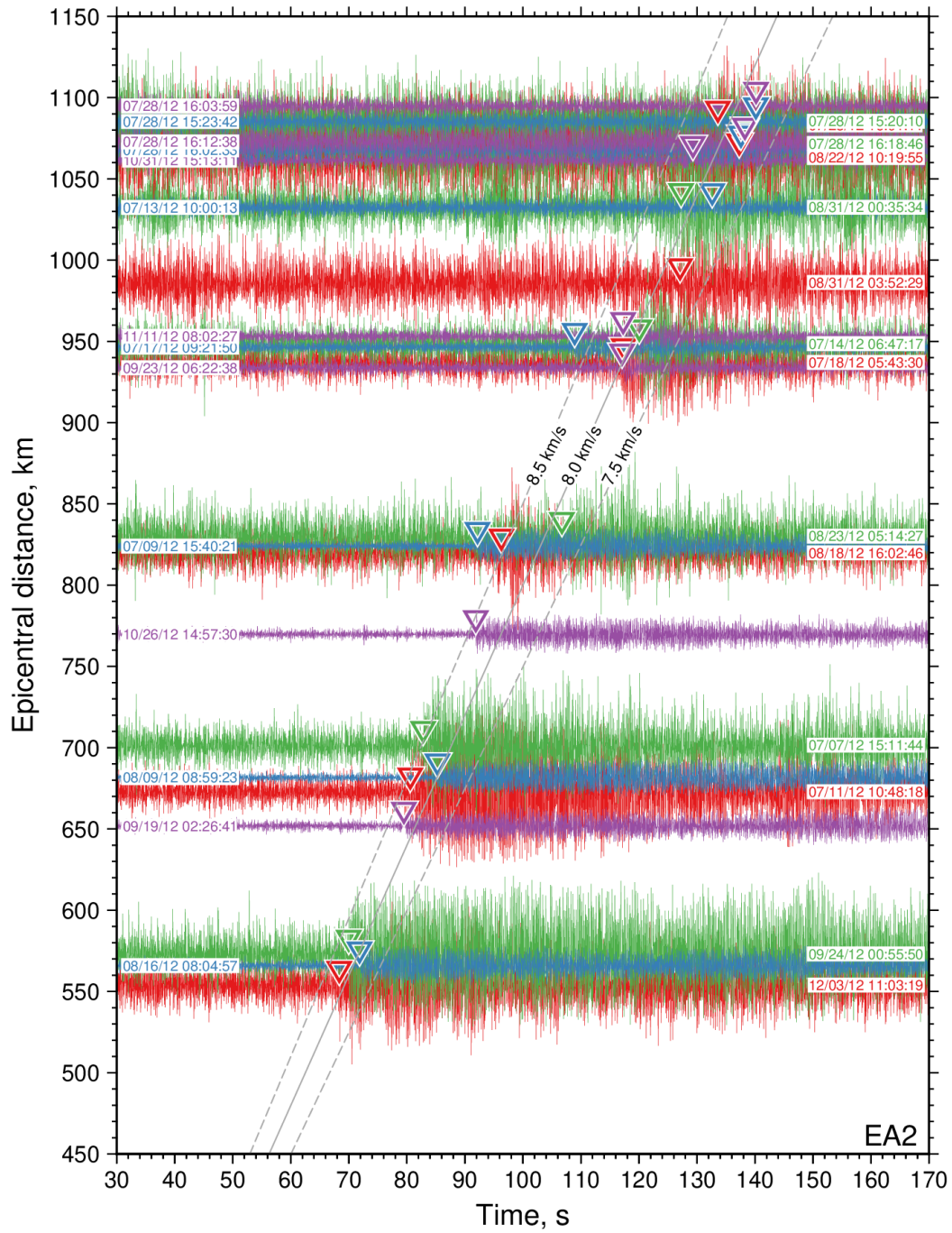
Figures S2. Common-receiver record sections for hydrophone H2; waveforms plotted with a 6–20 Hz Butterworth filter, amplitudes scaled to minimize overlap between adjacent traces; dashed solid/dashed lines show range of likely P_n velocities; colored triangles are P_n arrival picks.



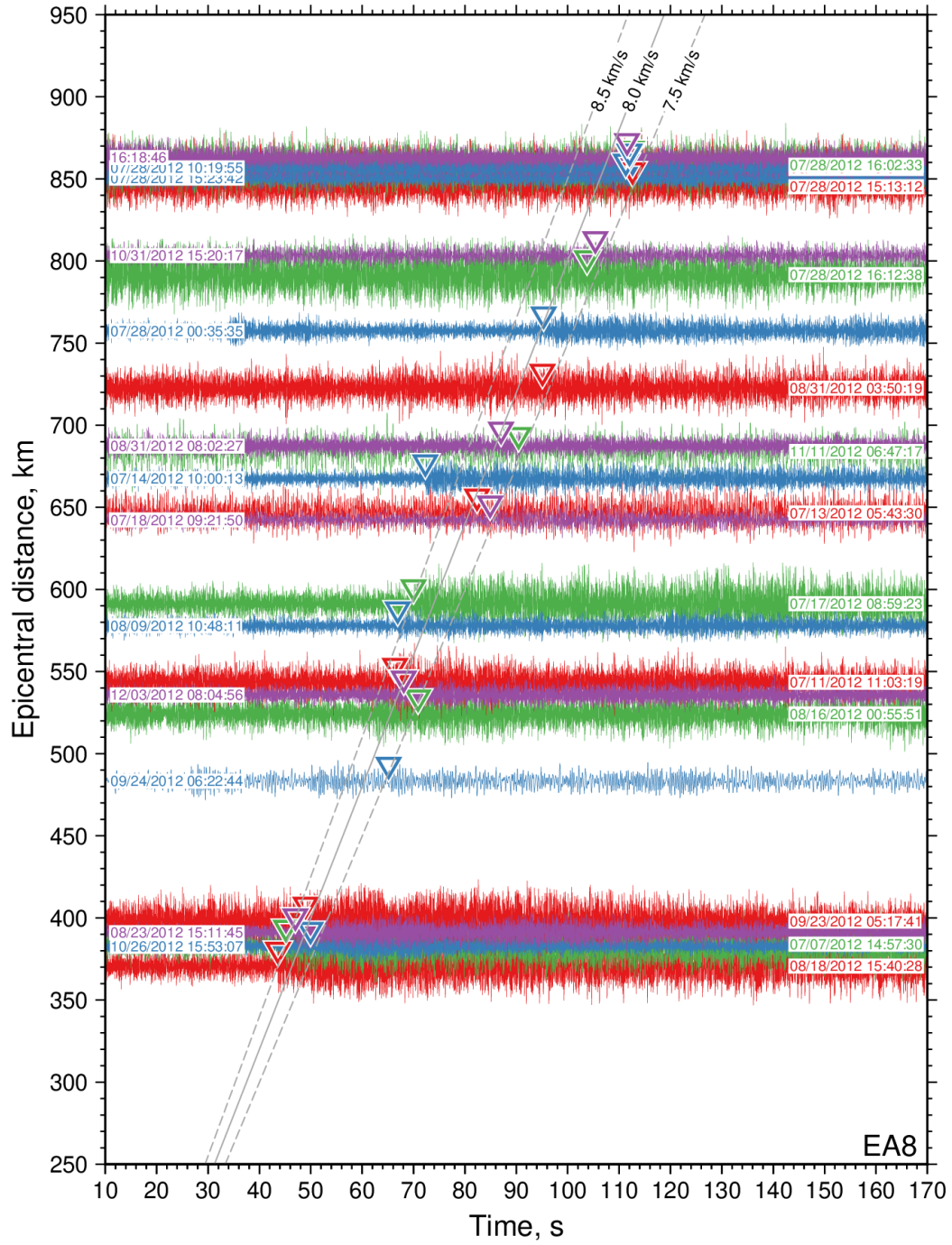
Figures S3. Common-receiver record sections for hydrophone H4; waveforms plotted with a 6–20 Hz Butterworth filter; amplitudes scaled to minimize overlap between adjacent traces; dashed solid/dashed lines show range of likely P_n velocities; colored triangles are P_n arrival picks.



Figures S4. Common-receiver record section for hydrophone H5; waveforms plotted with a 6–20 Hz Butterworth filter, amplitudes scaled to minimize overlap between adjacent traces; dashed solid/dashed lines show range of likely P_n velocities; colored triangles are P_n arrival picks.



Figures S5. Common-receiver record section for hydrophone EA2; waveforms plotted with a 6–20 Hz Butterworth filter, amplitudes scaled to minimize overlap between adjacent traces; dashed solid/dashed lines show range of likely *Pn* velocities; colored triangles are *Pn* arrival picks.



Figures S6. Common-receiver record section for hydrophone EA8; waveforms plotted with a 6–20 Hz Butterworth filter, amplitudes scaled to minimize overlap between adjacent traces; dashed solid/dashed lines show range of likely *Pn* velocities; colored triangles are *Pn* arrival picks.

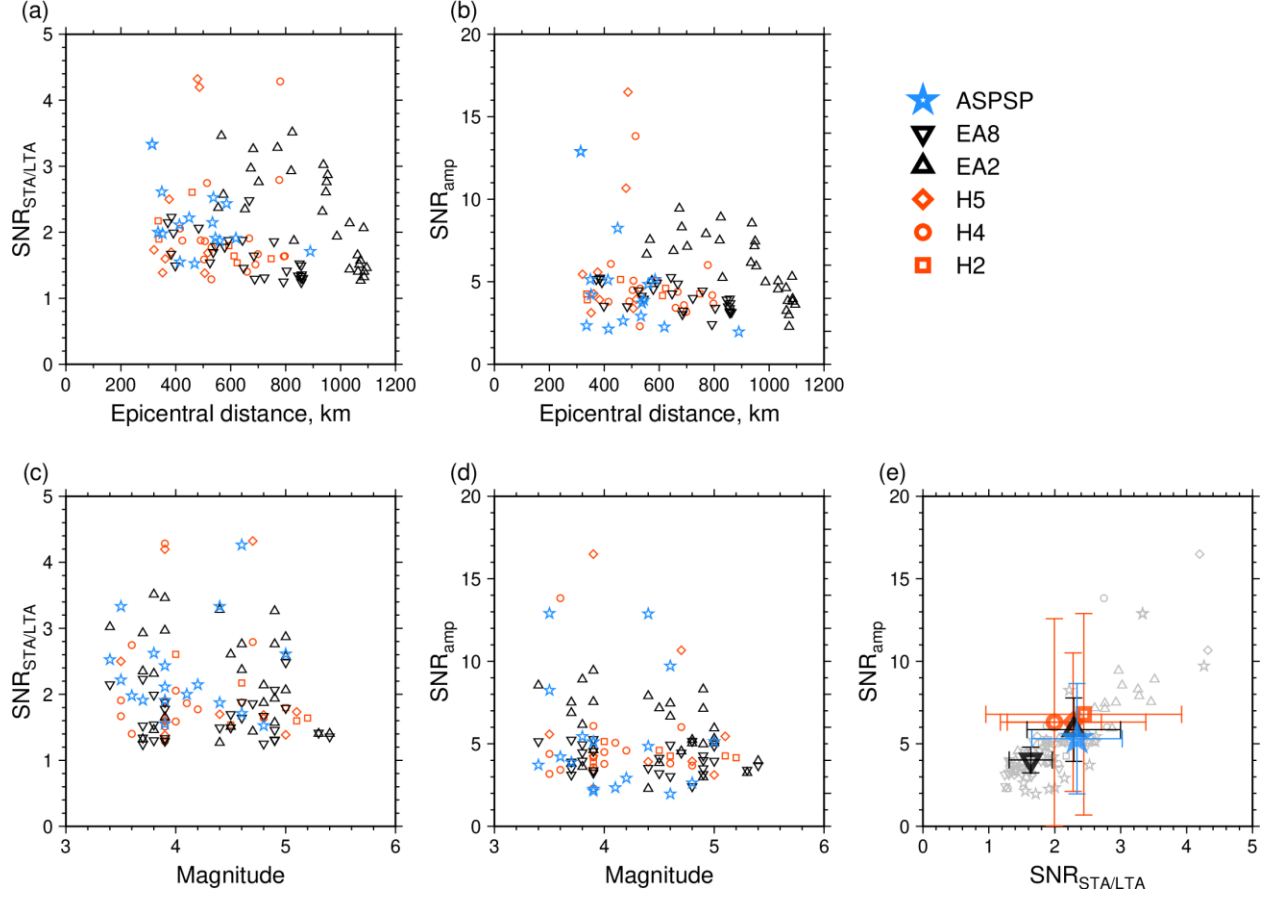


Figure S7. Noise characterization of P_n arrivals. **a)** Signal to noise ratio estimated from the ratio between short time (1 s window) and long time (20 s window) average amplitudes ($SNR_{STA/LTA}$), as a function of epicentral distance, key shows symbols used for stations. **b)** SNR estimated from ratio between the peak amplitude and the root mean square noise amplitude (SNR_{amp}), as a function of epicentral distance. **c)** $SNR_{STA/LTA}$ as a function of magnitude. **d)** SNR_{amp} as a function of magnitude. **e)** $SNR_{STA/LTA}$ vs. SNR_{amp} , symbols with error bars are mean values of SNR for each station ± 1 standard deviation.

References

- de Melo, G., and A. F. do Nascimento (2018). Earthquake Magnitude Relationships for the Saint Peter and Saint Paul Archipelago, Equatorial Atlantic, *Pure Appl. Geophys.* **175**, no. 3, 741–756, doi: 10.1007/s00024-017-1732-6.
- de Queiroz, D., A. F. do Nascimento, and M. Schimmel (2017). Microseismic noise in the Saint Peter and Saint Paul Archipelago, equatorial Atlantic, *J. South Am. Earth Sci.* **80**, 304–315, doi: 10.1016/j.jsames.2017.09.035.
- VanderBeek, B. P., and D. R. Toomey (2017). Shallow Mantle Anisotropy Beneath the Juan de Fuca Plate, *Geophys. Res. Lett.* **44**, no. 22, 11,382–11,389, doi: 10.1002/2017GL074769.

Author mailing addresses

Departamento de Geofísica, Federal University of Rio Grande do Norte, Natal, Brazil

(GWSM, AFN)

Institute of Geophysics and Planetary Physics, Scripps Institution of Oceanography, University of California, San Diego, CA, USA

(RPT)

NOAA, Pacific Marine Environmental Laboratory, Newport, OR, USA

(RPD)

National Science Foundation, Alexandria, VA, USA

(DKS)

Laboratoire Geosciences Ocean, CNRS and University of Brest

LGO-IUEM, rue Dumont Durville, 29280 Plouzane, France

(MM and JYR)